Reddy, G. Janardhana; Kethireddy, Bhaskerreddy; Kumar, Mahesh & Hoque, Mohammad Mainul. "A molecular dynamics study on transient non-Newtonian MHD Casson fluid flow dispersion over a radiative vertical cylinder with entropy heat generation" Published in the *Journal of Molecular Liquids*, Vol. 252, Issue February, p. 245-262, (2018).

Available from: http://dx.doi.org/10.1016/j.molliq.2017.12.077

A molecular dynamics study on transient non-Newtonian MHD Casson fluid flow dispersion over a radiative vertical cylinder with entropy heat generation

G. Janardhana Reddy[1, *], Bhaskerreddy Kethireddy[1], Mahesh Kumar[1] and Mohammad Mainul Hoque[2, *]

[1]*Department of Mathematics, Central University of Karnataka, Kalaburagi, India-585311*

[2]*Discipline of Chemical Engineering, University of Newcastle, Callaghan, NSW 2308, Australia*

Abstract:

In the present research article, the transient radiative free convective hydromagnetic Casson fluid flow past a vertical cylinder with entropy heat generation is analysed numerically. The mathematical model of this problem is constituted by highly time-dependent non-linear coupled equations and they are resolved by an efficient unconditionally stable implicit scheme. The time histories of average values of momentum and heat transport coefficients, entropy generation and Bejan number, as well as the steady-state flow variables are discussed for several values of non-dimensional parameters arising in the flow equations. The results indicate that entropy generation parameter and Bejan number upsurges with rising values of Casson fluid parameter, viscous dissipation parameter, group parameter and Grashof number, whereas the reverse trend is observed for radiation and magnetic parameters. Also, it is viewed that the variation of entropy and Bejan lines occur in the proximity of the hot cylindrical wall only. Finally, a comparison between the Casson and Newtonian fluid is made based on the obtained numerical results of the present study and this has important implications in industrial thermal materials processing operations.

Keywords: Casson fluid; entropy generation; MHD; vertical cylinder; thermal radiation; finite difference method.

[*]*Corresponding authors Emails:* gjr@cuk.ac.in, mohammadmainul.hoque@uon.edu.au

1. Introduction

A flow of viscous fluids subjected to the unsteady natural convection over a cylinder has a broad range of applications such as solar energy collectors, electromagnetics, transformers, nuclear reactors, wind energy, electrical heaters, oceanography, geomechanics etc. One such important mathematical model of free convective fluid flow past a uniformly heated vertical cylinder was analyzed by Sparrow and Gregg [1]. Lee et al. [2] studied the similar problem with power-law variation along the thin vertical cylinder. Such studies on rheological fluids are enviable for their growing importance in the science and engineering. But a very few non-Newtonian fluid flow problems in fluid mechanics received attention, because of their unique challenge to engineers, physicists, and mathematicians. Rani and Reddy [3] examined the time-dependent free convection flow of the non-Newtonian fluid past a cylinder with Dufour and Soret effects. Recently, Hirschhorn et al. [4] investigated the non-Newtonian magnetohydrodynamic (MHD) flow past a plate with slip boundary conditions.

Honey, jelly, concentrated fruit juices, soup, human blood, tomato sauce, etc. in the classification of polar fluid theories are under the category of Casson fluid, and this fluid fits the rheological data better than the typical viscoelastic models of many materials. This fluid defines as a shear thinning liquid which is assumed to have an infinite viscosity at zero rate of shear, a yield stress below which no flow occurs and zero viscosity at an infinite rate of shear [5]. Some researchers [6-7] studied the problem for Casson fluid flow with heat transfer past a stretching surface/sheet under different conditions. Time-dependent Casson fluid over a cone and plate under the effects of chemical reaction and radiation is studied by Mythili and Sivaraj [8]. Das et al. [9] studied the time-dependent MHD Casson fluid flow over a plate with chemical reaction and radiation. An MHD flow of Casson fluid over a sheet was investigated analytically by Nadeem et al. [10]. In recent times, Raju et al. [11] analyzed the natural convective heat transfer analysis of MHD unsteady Carreau nanofluid over a cone packed with alloy nanoparticles.

Also, the laws of thermodynamics and Newton's 2nd law of motion are the basic principles on which all the flow and heat transfer systems developed today. First law of thermodynamics provides information about the energy of the system quantitatively. On the other hand, the thermodynamics second law says that entire actuality processes are irretrievable and it is a useful tool to examine the entropy generation to assess the irreversibility in the system. Entropy production determines the irreversibility related to the natural processes such as a counter flow heat exchanger for gas to gas applications [12]. Currently, entropy analyses are used as a powerful tool for the determination of which procedure, system or installations are more effectual, and it has been the subject of various interests in several areas comparable to turbo machinery, porous media, electric cooling, heat transferring devices, and combustions. Few recent applications over entropy generation are pseudo-optimization design process in solar heat exchangers [13], minimizing lost available work during heat transfer processes [14] and multiphase flows [15]. The foremost of the energy-related applications, for example, cooling of modern electronic systems, solar energy collectors, and heat energy systems rely on entropy generation. Numerous studies [16-18] were carried out upon entropy generation with several flow formations. Several researchers studied the entropy generation concept related to the heat transfer problem for different geometries, particularly on the cylinder. Omid Mahian et al. [19] examined the entropy analysis between two vertical cylinders with different conditions in the presence of MHD. Also, studies on entropy generation past a stretching cylinder can be found in [20-22]. Bassam Abu-Hijleh et al. [23-25] analysed the entropy heat generation over a horizontal cylinder. Few studies present in the literature on thermodynamic analysis of fluid flow between rotating cylinders [26-28]. Recently, Jia Qing et al. [29] investigated the entropy generation on MHD Casson fluid flow over a porous surface. In addition, they have revealed the effect of entropy generation on nanofluid.

Also, the MHD fluid flow with thermal radiation effect is an important study in fluid dynamics due to its widespread applications in combustion, glass production, furnace design, the design of high temperature gas cooled nuclear reactors, nuclear reactor safety, fluidized bed heat exchanger, fire spreads, advanced energy conversion devices such as open cycle coal and natural gas fired MHD, solar fans, solar collectors, natural convection in cavities, turbid water bodies, photo chemical reactors and many others. To know this phenomenon, it is essential to study the behavior of flow profiles with MHD and thermal radiation effects. Few references related to the MHD and/or thermal radiative flows are listed here. Srinivas et al. [30] investigated the magnetized non-Newtonian fluid flow between two vertical rotating cylinders. They show that the external magnetic field force enhances the entropy generation rate. Also, entropy analysis of MHD flows due to cylinder geometry can be found in [31-32]. An interesting application was studied by Ramana Murthy and Srinivas [33] for the flow of two immiscible micropolar fluids with thermal radiation effects. Also, the analysis of entropy generation has been addressed in their study. For both MHD and radiation effects Guillermo Ibáñez et al. [34] studied the entropy analysis for a nanofluid in a porous microchannel. Similarly, a Casson fluid flow with MHD and/or radiation effects for different geometries is given in [35-36]. Recently, Ahmed [37] studied the heat and mass transfer characteristics in presence of radiation for a MHD fluid flow past a vertical porous plate. He also provided the analytical solutions for the flow-field equations using transformation techniques. Further, the radiative convection flow analysis of Casson fluid is shown in [38].

Based on the literature survey, it can be observed that very scant attention has been paid to the transient hydromagnetic Casson fluid flow past a radiative vertical cylinder with entropy heat generation. Hence, the specific aim of the present study is to investigate the second law of thermodynamic for a Casson fluid flow over a uniformly heated vertical cylinder with thermal radiation and MHD effects across the boundary layer region. A temperature at the wall is taken to be greater than that of surrounding fluid temperature. The transitory effects of the hydromagnetic Casson fluid flow with radiative entropy heat generation is studied for the momentum and heat transport coefficients for different control parameters and compared with the Newtonian fluid flow. The results obtained by implicit finite difference method are corroborated with the available existing results in the literature.

The organization of this research article is arranged in the following ways: Section 2 deals with the mathematical formulation and its non-dimensionalization for a Casson fluid flow over a semi-infinite vertical cylinder with thermal radiation and MHD effects. Also, average momentum and heat transport coefficients, entropy heat generation and Bejan number details are given. Section 3 dealt with the grid generation and numerical method to solve the flow-field equations. In the results and discussion section 4, the transient two-dimensional flow-field profiles, average wall and heat transfer rates are analysed in addition to entropy heat generation analysis and Bejan number. Also, the comparison between the flow due to the Casson and Newtonian fluids are shown and analysed. Finally, the concluding remarks are made in Section 5.

2. Mathematical modelling

Transient two-dimensional laminar buoyancy driven Casson fluid flow past a radiative vertical cylinder of radius r_0 with transversely applied magnetic field B_0 as shown in Fig. 1. The rectangular coordinate system is chosen wherein the axial coordinate (x-axis) is selected from the foremost verge of the cylinder and the radial coordinate (r-axis) is considered as normal to the x-axis. It is assumed that the neighboring fluid temperature is stationary and similar to that of free stream temperature T'_∞. At the outset, i.e. $t' = 0$, the temperature T'_∞ is uniform for the cylinder and surrounding fluid. Later ($t' > 0$), the temperature of the vertical cylinder is augmented to $T'_w (> T'_\infty)$ and preserved uniformly there afterward. The influence of viscous dissipation is assumed to be insignificant in the thermal equation, because the magnitude of velocity is expected to be minuscule in the flow regime.

Under the aforesaid assumptions, the incompressible Casson fluid is modelled by the following constitutive equations:

Law of conservation of mass:

$$\frac{\partial(ru)}{\partial x} + \frac{\partial(rv)}{\partial r} = 0 \tag{1}$$

Law of conservation of momentum:

$$\rho\left[\frac{\partial \mathbf{U}}{\partial t\prime} + (\mathbf{U}\,.\nabla)\mathbf{U}\right] = -\rho g - \nabla p + \mu\left(1+\frac{1}{\beta}\right)\nabla^2\mathbf{U} + (\,\mathbf{J}\times\mathbf{B}\,) \tag{2}$$

where, **J** and **B** are given by Ohm's law and Maxwell's equations, namely,

$\nabla\times\mathbf{E} = 0,\ \nabla\times\mathbf{H} = 4\pi\mathbf{J}\,,\ \nabla\times\mathbf{B} = 0,\ \ \mathbf{J} = \sigma[\mathbf{E} + \mathbf{U}\times\mathbf{B}]$

Here, **J** - current density, **E** - electric field, **H** - magnetic field, **B** - magnetic flux, **U** - velocity vector and σ - the electrical conductivity of the fluid.

The considered plate is under the effect of a transverse magnetic field with a uniform strength, B_0, as shown in Fig. 1. It is presumed that the magnetic Reynolds number is very small. Therefore, the interaction of the induced axial magnetic field with the motion of electrically-conducting couple stress fluid flow is expected to be minuscule compared to the interaction of the applied magnetic field. It is noted that further no external electric field is applied. With these assumptions, the magnetic field $\mathbf{J}\times\mathbf{B}$ of the body force term in momentum Eq. (2) reduces to $-\sigma B_0^2 u$, where B_0 is the intensity of the forced transverse magnetic field. Using Boussinesq's approximation the above Eq. (2) can be rewritten as

$$\rho\left(\frac{\partial u}{\partial t'} + u\frac{\partial u}{\partial x} + v\frac{\partial u}{\partial r}\right) = \mu\left(1+\frac{1}{\beta}\right)\left(\frac{\partial^2 u}{\partial r^2} + \frac{1}{r}\frac{\partial u}{\partial r}\right) + \rho g\beta_T(T' - T'_\infty) - \sigma B_0^2 u \tag{3}$$

where $\beta = \mu_B\sqrt{2\pi_c}/p_y$ is the Casson fluid parameter.

The rheological model of an incompressible flow of a Casson fluid can be written as follows (Casson [39]; Hakeem et al. [40]):

$$\tau_{ij} = \begin{cases} 2\left(\mu_B + p_y/\sqrt{2\pi}\right)e_{ij}\,, & \pi > \pi_c \\ 2\left(\mu_B + p_y/\sqrt{2\pi_c}\right)e_{ij}\,, & \pi < \pi_c \end{cases} \tag{4}$$

where, τ_{ij} and e_{ij} represents the $(i, j)^{\text{th}}$ component of the shear stress tensor and deformation rate respectively. p_y is the yield stress of the fluid and $\pi(= e_{ij}e_{ij})$ denotes product of the component of deformation rate with itself, π_c denotes a critical value of this product based on the non-Newtonian model and μ_B is plastic dynamic viscosity of the non-Newtonian fluid. So, if a shear stress is less than the yield stress applied to the fluid, it acts like a solid, whereas if a shear stress is exceeding the applied yield stress, it starts to move.

Law of conservation of Energy:

$$\frac{\partial T'}{\partial t'} + u\frac{\partial T'}{\partial x} + v\frac{\partial T'}{\partial r} = \frac{\alpha}{r}\frac{\partial}{\partial r}\left(r\frac{\partial T'}{\partial r}\right) + \frac{\upsilon}{c_p}\left(1 + \frac{1}{\beta}\right)\left(\frac{\partial u}{\partial r}\right)^2 - \frac{1}{\rho c_p}\frac{\partial}{\partial r}(rq_r) \tag{5}$$

Based on the Rosseland approximation (Brewster [41]), the radiative heat flux q_r is given by

$$q_r = -\frac{4\sigma^*}{3\kappa^*}\frac{\partial T'^4}{\partial r} \tag{6}$$

where σ^* is the Stefan-Boltzmann constant and κ^* is the mean absorption coefficient. The temperature differences within the flow are considered to be sufficiently small that T'^4 may be expressed as a linear function of the temperature. Expanding T'^4 using the Taylor series and neglecting the higher order terms yields

$$T'^4 \cong 4T_\infty'^3 T' - 3T_\infty'^4 \tag{7}$$

In view of Eqs. (6) and (7), Eq. (5) reduces to

$$\frac{\partial T'}{\partial t'} + u\frac{\partial T'}{\partial x} + v\frac{\partial T'}{\partial y} = \frac{\alpha}{r}\frac{\partial}{\partial r}\left(r\frac{\partial T'}{\partial r}\right) + \frac{\upsilon}{c_p}\left(1 + \frac{1}{\beta}\right)\left(\frac{\partial u}{\partial r}\right)^2 + \left(\frac{16\sigma^* T_\infty'^3}{3\rho c_p \kappa^*}\right)\frac{1}{r}\frac{\partial}{\partial r}\left(r\frac{\partial T'}{\partial r}\right) \tag{8}$$

The resultant initial and boundary conditions are given by

$$\begin{aligned} &t' \le 0: T' = T_\infty',\, u = 0, v = 0 && \forall\, x \text{ and } r \\ &t' > 0: T' = T_w',\, u = 0, v = 0 && \text{at } r = r_0 \\ &\qquad\quad T' = T_\infty', u = 0, v = 0 && \text{at } x = 0 \end{aligned} \tag{9}$$

$$T' \to T'_\infty, u \to 0, v \to 0 \qquad \text{as } r \to \infty$$

Initiating the subsequent non-dimensional quantities

$$U = Gr^{-1}\frac{ur_0}{\upsilon},\ V = \frac{vr_0}{\upsilon},\ t = \frac{\upsilon t'}{r_0^2},\ X = Gr^{-1}\frac{x}{r_0},\ Pr = \frac{\upsilon}{\alpha},\ \theta = \frac{T'-T'_\infty}{T'_w-T'_\infty},\ Gr = \frac{g\beta_T r_0^3(T'_w-T'_\infty)}{\upsilon^2},$$

$$R = \frac{r}{r_0},\ Br = \frac{\mu\upsilon^2}{k(T'_w-T'_\infty)r_0^2},\ M = \frac{\sigma B_0^2 r_0^2}{\rho\upsilon},\ \varepsilon_0 = \frac{\upsilon^2}{c_p(T'_w-T'_\infty)r_0^2},\ N = \frac{\kappa^* k}{4\sigma^* {T'_\infty}^3} \tag{10}$$

(for the above symbols refer nomenclature) in the Eqs. (1), (3), (8) and (9), they reduce to subsequent form

$$\frac{\partial U}{\partial X} + \frac{\partial V}{\partial R} + \frac{V}{R} = 0 \tag{11}$$

$$\frac{\partial U}{\partial t} + U\frac{\partial U}{\partial X} + V\frac{\partial U}{\partial R} = \theta + \left(1+\frac{1}{\beta}\right)\left(\frac{\partial^2 U}{\partial R^2} + \frac{1}{R}\frac{\partial U}{\partial R}\right) - MU \tag{12}$$

$$\frac{\partial \theta}{\partial t} + U\frac{\partial \theta}{\partial X} + V\frac{\partial \theta}{\partial R} = \frac{1}{Pr}\left(1+\frac{4}{3N}\right)\left(\frac{\partial^2 \theta}{\partial R^2} + \frac{1}{R}\frac{\partial \theta}{\partial R}\right) + \left(1+\frac{1}{\beta}\right)(Gr)^2\varepsilon_0\left(\frac{\partial U}{\partial R}\right)^2 \tag{13}$$

$$t \le 0: \theta = 0, U = 0, V = 0, \qquad \forall\, X \text{ and } R$$

$$t > 0: \theta = 1, U = 0, V = 0 \qquad \text{at } R = 1$$

$$\theta = 0, U = 0, V = 0 \qquad \text{at } X = 0$$

$$\theta \to 0, U \to 0, V \to 0 \qquad \text{as } R \to \infty \tag{14}$$

2.1. *Friction and heat transport coefficients*

The momentum and heat transport coefficients are significant parameters in the heat transfer studies due to their direct involvement in the convection. In the present study, the non-dimensional average momentum and heat transport coefficients are defined as

$$\overline{C_f} = \left(1+\frac{1}{\beta}\right)\int_0^1 \left(\frac{\partial U}{\partial R}\right)_{R=1} dX \tag{15}$$

$$\overline{Nu} = -\int_0^1 \left(\frac{\partial \theta}{\partial R}\right)_{R=1} dX \tag{16}$$

The above coefficients are calculated using the five-point approximation and Newton–Cotes quadrature formula.

2.2. *Entropy heat generation analysis and Bejan number*

The entropy generation for radiative magnetohydrodynamic Casson fluid per unit volume with constant density is given by

$$S_{gen} = \frac{k}{T_{\infty}'^{2}}\left(\frac{\partial T'}{\partial r}\right)^2 + \frac{\mu}{T_{\infty}'}\left(1+\frac{1}{\beta}\right)\left(\frac{\partial u}{\partial r}\right)^2 + \frac{\sigma B_0^2 u^2}{T_{\infty}'} - \frac{1}{T_{\infty}'^{2}}\left(\frac{\partial T'}{\partial r}\right) q_r \tag{17}$$

Using Eqs. (6) and (7), Eq. (17) reduces to

$$S_{gen} = \frac{k}{T_{\infty}'^{2}}\left(\frac{\partial T'}{\partial r}\right)^2 + \frac{\mu}{T_{\infty}'}\left(1+\frac{1}{\beta}\right)\left(\frac{\partial u}{\partial r}\right)^2 + \frac{\sigma B_0^2 u^2}{T_{\infty}'} + \frac{1}{T_{\infty}'}\left(\frac{16\sigma^* T_{\infty}'^{3}}{3\kappa^*}\right)\left(\frac{\partial T'}{\partial r}\right)^2 \tag{18}$$

The equation (18) can be rewritten as

$$S_{gen} = S_1 + S_2 + S_3 + S_4$$

where $S_1\left[= \frac{k}{T_{\infty}'^{2}}\left(\frac{\partial T'}{\partial r}\right)^2\right]$ signifies the entropy generation due to the heat flow, $S_2 = \left[\frac{\mu}{T_{\infty}'}\left(1+\frac{1}{\beta}\right)\left(\frac{\partial u}{\partial r}\right)^2\right]$ denotes the entropy generation due to the viscous dissipation for a constant density, $S_3\left[= \frac{\sigma B_0^2 u^2}{T_{\infty}'}\right]$ denotes the entropy generation due to the MHD and $S_4\left[= \frac{1}{T_{\infty}'}\left(\frac{16\sigma^* T_{\infty}'^{3}}{3\kappa^*}\right)\left(\frac{\partial T'}{\partial r}\right)^2\right]$ denotes the entropy generation due to the thermal radiation.

The non-dimensional entropy heat generation parameter *Ns* is defined as the ratio of the volumetric entropy heat generation rate to the characteristic entropy heat generation rate. Accordingly, the entropy heat generation parameter is written as [42]:

$$Ns = \left(1+\frac{4}{3N}\right)\left(\frac{\partial \theta}{\partial R}\right)^2 + \frac{Br(Gr)^2}{\Theta}\left(1+\frac{1}{\beta}\right)\left(\frac{\partial U}{\partial R}\right)^2 + \frac{Br(Gr)^2}{\Theta} M U^2 \tag{19}$$

where $\Theta = \frac{(T_w' - T_\infty')}{T_\infty'}$ is the non-dimensional temperature difference and $\frac{k(T_w'-T_\infty')^2}{T_\infty'^{2} r_0^2}$ is the characteristic entropy heat generation.

The Eq. (19) can be rewritten in the following form

$$Ns = N_1 + N_2 + N_3 \tag{20}$$

where $N_1 = \left(1+\frac{4}{3N}\right)\left(\frac{\partial\theta}{\partial R}\right)^2$, $N_2 = \frac{Br(Gr)^2}{\Theta}\left(1+\frac{1}{\beta}\right)\left(\frac{\partial U}{\partial R}\right)^2$ and $N_3 = \frac{Br(Gr)^2}{\Theta}MU^2$ designate the irreversibility owing to thermal radiative heat transfer, fluid friction (viscous dissipation) and entropy generation due to the magnetic field, respectively.

To assess the irreversibility distribution, the parameter Be (Bejan number) is defined as the ratio of entropy heat generation due to heat transfer to the overall entropy heat production and can be expressed as:

$$Be = \frac{N_1}{N_1+N_2+N_3} \tag{21}$$

From the Eq. (21), it is understood that the Bejan number lies between 0 to 1 i.e. $0 \leq Be \leq 1$. Consequently, $Be = 0$ reveals that the parameters N_2 and N_3 dominates the parameter N_1, whereas $Be = 1$ indicates that the parameter N_1 dominates the parameters N_2 and N_3. It is obvious that at $Be = 0.5$, the contribution of fluid friction and magnetic field in the entropy generation production is equal to irreversibility due to the heat transfer i.e. $N_2 + N_3 = N_1$.

3. Finite difference solution procedure

To elucidate the above governing time-dependent mathematical Eqs. (11) - (13) an unconditionally stable finite difference iteration scheme such as Crank-Nicolson type is employed. The finite difference equations to the above Eqs. (11), (12) and (13) are as follows:

$$\frac{U_{l,m}^{n+1}-U_{l-1,m}^{n+1}+U_{l,m}^{n}-U_{l-1,m}^{n}}{2\Delta X}+\frac{V_{l,m}^{n+1}-V_{l,m-1}^{n+1}+V_{l,m}^{n}-V_{l,m-1}^{n}}{2\Delta R}+(JR)V_{l,m}^{n+1}=0 \tag{22}$$

$$\frac{U_{l,m}^{n+1}-U_{l,m}^{n}}{\Delta t}+\frac{U_{l,m}^{n}}{2\Delta X}\left(U_{l,m}^{n+1}-U_{l-1,m}^{n+1}+U_{l,m}^{n}-U_{l-1,m}^{n}\right)+\frac{V_{l,m}^{n}}{4\Delta R}\left(U_{l,m}^{n+1}-U_{l,m-1}^{n+1}+U_{l,m}^{n}-U_{l,m-1}^{n}\right)$$

$$=\frac{\theta_{l,m}^{n+1}+\theta_{l,m}^{n}}{2}+JR\left(1+\frac{1}{\beta}\right)\left(\frac{U_{l,m+1}^{n+1}-U_{l,m-1}^{n+1}+U_{l,m+1}^{n}-U_{l,m-1}^{n}}{4(\Delta R)}\right)+$$

$$\left(1+\frac{1}{\beta}\right)\left(\frac{U_{l,m+1}^{n+1}-2U_{l,m}^{n+1}+U_{l,m-1}^{n+1}+U_{l,m+1}^{n}-2U_{l,m}^{n}+U_{l,m-1}^{n}}{2(\Delta R)^2}\right)-M\frac{\left(U_{l,m}^{n+1}+U_{l,m}^{n+1}\right)}{2} \tag{23}$$

$$\frac{\theta_{l,m}^{n+1}-\theta_{l,m}^{n}}{\Delta t}+\frac{U_{l,m}^{n}}{2\Delta X}\left(\theta_{l,m}^{n+1}-\theta_{l-1,m}^{n+1}+\theta_{l,m}^{n}-\theta_{l-1,m}^{n}\right)+\frac{V_{l,m}^{n}}{4\Delta R}\left(\theta_{l,m}^{n+1}-\theta_{l-1,m}^{n+1}+\theta_{l,m}^{n}-\theta_{l-1,m}^{n}\right)$$

$$= \left(1+\frac{4}{3N}\right)\left\{\left[\frac{\theta_{l,m+1}^{n+1}-2\theta_{l,m}^{n+1}+\theta_{l,m-1}^{n+1}+\theta_{l,m+1}^{n}-2\theta_{l,m}^{n}+\theta_{l,m-1}^{n}}{2Pr(\Delta R)^2}\right]+(JR)\left[\frac{\theta_{l,m+1}^{n+1}-\theta_{l,m-1}^{n+1}+\theta_{l,m+1}^{n}-\theta_{l,m-1}^{n}}{4Pr(\Delta R)}\right]\right\}$$

$$+\left(1+\frac{1}{\beta}\right)(Gr)^2\varepsilon_0\left(\frac{U_{l,m+1}^{n+1}-U_{l,m-1}^{n+1}+U_{l,m+1}^{n}-U_{l,m-1}^{n}}{4(\Delta R)}\right)\left(\frac{U_{l,m+1}^{n}-U_{l,m-1}^{n}}{2(\Delta R)}\right) \tag{24}$$

where $JR = \frac{1}{[1+(m-1)\Delta R]}$.

The results of these finite difference equations obtained in the rectangular grid with $X_{max} = 1$, $X_{min} = 0$, $R_{max} = 20$ and $R_{min} = 1$ where R_{max} relates to $R = \infty$ which lies far away from the heat and momentum transport boundary layers.

3.1 Validation of the numerical code using grid independence study

To have an economical consistent grid scheme for the reckonings, a grid independency test has been conducted using four different grid sizes of 25 × 125, 50 × 250, 100 × 500 and 200 × 1000. The values of the average skin-friction coefficient ($\overline{C_f}$) and Nusselt number ($\overline{Nu}$) on the boundary $R = 1$ for the aforesaid grid sizes are shown in Table 1. It is evident that the values estimated for the grid size of 100 × 500 differ in the fourth decimal place with the grid size of 25 × 125 and 50 × 250 while 200 × 1000 does not have significant effect on the results of $\overline{C_f}$ and $\overline{Nu}$. Hence, according to this observation, a uniform grid size of 100 × 500 was selected for all subsequent simulation with the mesh sizes of 0.01 and 0.03 along the axial and radial directions, respectively. Similarly, to produce a reliable result with respect to time, a grid independent tests have been done for different time step sizes as shown in Table 2, where the time step size Δt $(t = n\Delta t, n = 0, 1, 2, \ldots)$ fixed as 0.01.

The finite difference procedure begins by computing the thermal Eq. (13), which gives the temperature field. Then, solving the momentum transport and conservation of mass equations (12) and (11) provide the solution of the velocity field. Eqs. (23) - (24) at the $(n+1)^{\text{th}}$ iteration using the known n^{th} iteration values are specified in the following tridiagonal form:

$$a_{l,m}\Phi_{l,m-1}^{n+1} + b_{l,m}\Phi_{l,m}^{n+1} + c_{l,m}\Phi_{l,m+1}^{n+1} = d_{l,m}^{n}$$

where Φ denotes the time-dependent flow field variables θ and U. Therefore, Eqs. (23) - (24) on a particular l-level at every internal nodal point comprise a system of tridiagonal equations. The detailed description of this finite difference scheme can be found in [43-47].

4. Results and discussion

To study the unsteady behaviour of the virtual flow-field variables, such as temperature and velocity, their values are illustrated at one position, which are neighbouring to the hot cylindrical wall. The time-independent state temperature and velocity profiles are presented along the radial coordinate at X=1.0.

In order to validate the present numerical results, in Fig. 2 the flow-field variables of Newtonian fluids are compared with the results of Lee et al. [2] for $Pr = 0.7$, $\beta = \infty, \varepsilon_0 = M = N = 0.0$. The outcomes are found to be in good covenant. It is evident that the present results make a good agreement with the results of Lee et al. [2]. These results confirm the validity and accurateness of the current numerical scheme. It is noted that no experimental works are available till date to the best of the authors' knowledge, so, the comparison between the present study and experimental work could not be possible. The simulated results are represented to describe the variation of the dimensionless flow variables, entropy generation number (Ns) and Bejan number (Be) which are examined along with average skin-friction and heat transport coefficients for different flow control parameters arise in this problem. Such variations are plotted and conferred in the following paragraphs.

The influences of dimensionless flow parameters on the velocity constituents are discussed and analysed in Fig. 3. The unsteady velocity (U) against time (t) at (1, 4.03) location for distinct values of Casson fluid parameter (β) and viscous dissipation parameter (ε_0) is graphically presented in Fig. 3a. Here, the position (1, 4.03) has been chosen to be the location of highest velocity based on the time-independent velocity profiles shown in Figs. 4a & 4b. Figs. 3a and 3b depicts that the variation of β & ε_0 and M & N, respectively. From Figs. 3a and

3b, for all values of control parameters, excluding M, the velocity enhances with time, attains the temporal peak, then marginally decreases and finally leads to the time-independent state. From Fig. 3a it is seen that the transient U profile increases with the increasing values of β or ε_0 at the neighbourhood of the cylinder wall. The incentive behind this increment is that increasing β values decreases the size of the velocity diffusion term in Eq. (12) and thus, there is a lesser amount of resistance to the fluid flow in the province of the temporal peak of velocity. From Fig. 3a it is perceived that when $t << 1.3$, the conduction dominates the heat transfer. Subsequently, there occurs a time stage where the heat transfer rate is influenced by the effect of natural convection of Casson fluid with raising upward velocities with respect to time. Later, before attaining the steady-state, the velocities get overshoot. As illustrated in Fig. 3a it is observed that initially transient velocity profiles concurred with each other and then diverge after some time. Also from Fig. 3a it is noticed that as β upsurges the time to accomplish the steady-state increases and reverse trend is noticed for ε_0. From Fig. 3a it is noticed that as β or ε_0 increases, the time to accomplish the temporal peak decreases. Fig. 3b shows the similar transient features as shown in Fig. 3a, but initially the U curves for all values of β & ε_0 coincided with each other and diverges after some time. In the Fig. 3b it is perceived that as M or N upsurges, the velocity decreases, since a higher M value means a higher force resisting the flow and a higher N value allows higher thermal transport across the boundary. Similarly, the velocity at other locations also exhibits somewhat similar transient behaviour. From Fig. 3b it is noticed that as M or N upsurges the time to accomplish the steady-state increases. The same observation is tabulated in Table 3.

Figs. 4a and 4b elucidate the time independent-state U profiles for the variation of β & ε_0 and M & N against R respectively. It can be observed that the U profile in these figures start with the no-slip boundary condition, reaches its peak and then shrink to zero along the R coordinate satisfying the far-away boundary conditions. Also, in the neighbourhood of the hot cylindrical wall, it is noted that the magnitude of non-dimensional axial velocity (U) is suddenly amplifying as R rises from $R_{\min}$ (=1). In Fig. 4a the time-independent U curves in the region near to the wall, i.e., $1.0<R<5.71$ has increased trend for increasing values of β and opposite trend is noted in the region far from the hot wall (i.e., $R > 5.71$), i.e., in the zone which is away from the hot wall, the peak value of velocity moves towards with augmented velocity boundary layer thickness. This is because augmenting the values of β leads to the decrease of the total viscosity in Casson fluid flow, thus increasing the peak fluid velocity. Also, the velocity curves increase as ε_0 increases. From Fig. 4b it is noticed that the magnitude of the time-independent velocity curves decreases as M amplifies. This implies that magnetic field suppresses fluid velocity. This is due to the fact that the application of the magnetic field of an electrically conducting fluid gives rise to resistive force which is known as Lorentz force. Also, the boundary layer thickness increases with increasing value of the magnetic parameter. Here, the effect of N on the velocity profile can be considered. In a typical natural convection without radiative effect, the thermal term $\left(\frac{\partial^2\theta}{\partial R^2} + \frac{1}{R}\frac{\partial\theta}{\partial R}\right)$ makes the convective term positive owing to its own positive value. With the radiative effect in the present problem a higher value N yields a smaller convective term, resulting in a profile of low temperature at $X = 1.0$ (see Fig. 5) and, therefore, yielding a lower velocity.

Figs. 5a-b depicts the variation of β & ε_0 and M & N on unsteady temperature profile (θ) against the time (t) at the location (1, 1.34), respectively. From these figures it is clear that the unsteady temperature profile is increasing with time, reaches the peak value, then decreases and again slightly increases, and finally reached the time-independent state asymptotically. It is worth to note that this transient phenomenon of the temperature is also evident at other locations. During the early period, the nature of the time-dependent temperature profiles is mainly noticeable. From Fig. 5a it is noticed that for different values of β or ε_0, the time-dependent temperature profiles firstly overlap with each other and then differ after a time. Also, it is noted that the time to attain the temporal peak decreases as β or ε_0 amplifies for all transient θ curves (see Fig. 5a) and reverse trend holds true for Fig. 5b. From Fig. 5a, it is observed that the θ profile decreases with increasing the value of β and reverse trend is noted for ε_0. Similarly, the θ profile is rapidly increasing as *M* increases and opposite behaviours also noticed for *N* (Fig. 5b).

Fig. 6a-b presents the steady-state non-dimensional θ profiles as a function of radial coordinate for various values of β & ε_0 and *M* & *N* against *R*, respectively. These patterns begin with the boundary value of $\theta = 1$ and then reduce to zero. It is observed that an upsurge in ε_0 results upsurge in the θ profile and reverse trend is noted for β (Fig. 6a). Similar trends are observed for *M* and *N* (Fig. 6b), respectively. The phenomenon that the temperature decreases with an increase in the *N* value is explained before. As the value of *N* increases from 0.2 to 0.5 with fixed *M* (= 1.0), the temperature decreases markedly. As a result, the thermal boundary layer thickness is decreased due to a rise in *N* values. Smaller *M* and larger *N* values give rise to the thinner thermal boundary layer, since a smaller *M* value implies less-suppressed boundary layer flow, and a larger *N* value means smaller thermal convection.

Figs. 7-8 illustrates the average skin-friction and heat transport coefficients as a function of time (*t*) for various parametric values such as β & ε_0 and *M* & *N*, respectively. In Fig. 7a, at first the $\overline{C_f}$ increases with *t*, and after a certain lapse of time, they become independent of time throughout the transient period. This is true since the buoyancy-induced flow-field velocity is comparatively small at initial time-dependent period, as perceived in Fig. 3, and the average momentum transport coefficient remains small, as observed in Fig. 7. Also, it is seen that $\overline{C_f}$ amplifies with augmenting the values of ε_0 and reverse trend is noted for β. Also, increasing the values of β the $\overline{C_f}$ decreases. This is true since as β increases the velocity increases (Refer Fig. 4) and the term $\left(1 + \frac{1}{\beta}\right)$ decreases, which give the decreased velocity gradient and causes decrease in $\overline{C_f}$ (Refer Eq. (15)). Also, from Fig. 7a it is noticed that $\overline{C_f}$ upsurges as ε_0 upsurges. Fig. 7b demonstrates that rising values of M and N give the decreasing value in $\overline{C_f}$ and this is in line with the time-dependent velocity profile mentioned in Fig. 3.

Figs. 8a and 8b illustrate that, in the beginning time, $\overline{Nu}$ decreases drastically, then slightly increasing and again reach the time independent-state. Also, it is noted that initially the $\overline{Nu}$ curves coincided with each other and diverged after some time. More clearly, these figures show that in the starting time the heat conduction only occurs, and are more dominant than the convection. Here it is perceived that $\overline{Nu}$ decreases with augmenting values of ε_0 and reverse trend is noted for β as shown in Fig. 8a. This is same as reflected in reverse trend in the transient temperature profile shown in Fig. 5, since $\overline{Nu}$ gives the negative temperature gradient values on the hot wall (Refer Eq. 16). From Fig. 8b it is observed that as the M increases, the effect of the Lorentz force on the flow field decreases, and hence the flow velocity increases in the boundary layer region. This is associated with higher temperature gradients at the walls, resulting in higher heat transfer rates. It is observed that at short times after $t = 0$, the average Nusselt numbers are almost the same for the various parameters which indicate that initially there is only heat conduction. Increasing N speeds up the spatial decay of the temperature field near the heated surface, yielding an increase in the rate of heat transfer.

The influence of the different flow-field parameters upon entropy generation (Ns) versus time (t) at the location (1, 2.10) is presented in Figs. 9a-c. The variation of Casson fluid parameter (β) & viscous dissipation parameter (ε_0), magnetic parameter (M) & radiation parameter (N) and group parameter ($Br\Theta^{-1}$) & Grashof number (Gr) on transient Ns are depicted in Figs. 9a – 9c, respectively. From these plots, it is ascertained that, initially, the Ns curves increase radically, then decreases, again upsurges, reach a temporal peak, and finally become independent of time. The important observation noted here is that in the beginning of time all the Ns curves concurred with each other and splits after some time for all values of control parameters. This indicates that at initial time levels (i.e., $t < 0.25$) the conduction is more dominated than the heat transfer. After some time, there occurs a stage when the rate of heat transfer is swayed by the influence of free convection with rising entropy production upward with time. As soon as this transient period has nearly completed and just before reaching the time-independent state, there occur overshoots of the entropy profile. From Figs. 9a and 9c, it is noted that the *Ns* increases with increasing β or ε_0 or $Br\Theta^{-1}$or *Gr*, respectively. Also, in Fig. 9b it is perceived that as *M* or *N* increases the transient entropy heat generation number decreases. From the Figs. 9a and 9b, it is understood that the time to achieve temporal peak is same for all increasing values of β or ε_0 or *M*. Similarly, in the Figs. 9b and 9c, the time to attain temporal peak increases as *N* increases and decreases as $Br\Theta^{-1}$ or *Gr* increases. In the Fig. 9c, it is ascertained that, initially, the *Ns* curves increases radically, then decreases, again upsurges, reach a temporal peak, and finally become independent of time. It is worth to mention that in the beginning of time all the *Ns* curves concurred with each other and splits after some time for all values of control parameters. The time taken to attain the temporal peak slightly decreases as $Br\Theta^{-1}$ or *Gr* increases. Thus, amplifying values of Grashof number results in more entropy production.

The simulated time-independent dimensionless *Ns* profile for different control parameters such as β & ε_0, *M* & *N* and $Br\Theta^{-1}$ & *Gr* along the radial direction at $X = 1.0$ are revealed in Figs. 10a-c, respectively. It is remarked that as the radial position increases, the *Ns* curves drastically increases and achieves the peak value, then suddenly decreases and reaches monotonically to zero. Here it can be noted that the *Ns* curves are sharpened at peak value in the neighbourhood of the hot cylindrical wall. However, the velocity curves get smooth at peak value which is shown in the Figs 4a and 4b. Also, it is identified that the entropy production gets thinner boundary layer for all values of control parameters. This is as a result of higher entropy production is observed adjacent to the hot wall which yields thinner boundary layer.

From Fig. 10a, it is perceived that for augmenting the values of β, the steady-state *Ns* curves increase in the interval $R \in [1, 1.45]$ then decreases when *R* > 1.45 and for augmenting values of ε_0, the steady-state *Ns* curves decrease (i.e., in the interval $R \in [1, 1.6]$), then increases when *R* > 1.6. This is because of a reduction in the heat transport coefficient near to the tropical region causes decrease in *Ns* (Refer Fig. 8a). From Fig. 10b, the entropy profiles are noticed to be decreasing with increase value of *M* or *N*. It is observed that as *M* or *N* upsurges the entropy curves coincided with each other having a slight variation as *R* amplifies from R_{min}=1. From Figs 10a and 10b, it is identified that the time taken to achieve the steady-state decreases as ε_0, upsurges, and for the β or *M* or *N* this trend is reversed. Fig. 10c reveal that in the neighbourhood of a hot cylindrical wall, the entropy increases rapidly, then decrease drastically, and approach to zero along the radial coordinate. It is also noted that for augmenting values of $Br\Theta^{-1}$ or *Gr*, the *Ns* curves increases (Fig. 10c). This is because the entropy production due to the fluid friction increases for larger values of Grashof number or group parameter. Also, it is mentioned that the time needed to attain steady-state rises for rising values of $Br\Theta^{-1}$ or *Gr* (see, Fig. 10c).

The influence of the different flow-field parameters upon Bejan number (*Be*) versus time (*t*) at the location (1, 2.10) are presented in Figs. 11a-c. The variation of Casson fluid parameter (β), viscous dissipation parameter (ε_0), magnatic parameter (*M*), Radiation parameter (*N*), group parameter ($Br\Theta^{-1}$) and Grashof number (*Gr*) on a transient *(Be)* are depicted in Figs. 11a – 11c, respectively. These data show that initially *Be* start with zero value, increases drastically with time and attains the peak value, then drops marginally, and finally becomes independent of time after slight fluctuation. From Fig. 11a, it is seen that as β or ε_0 amplifies the Bejan number upsurges. From Fig. 11b it is viewed that increasing *M* or *N* gives the decreasing values in *Be*. The important observation in these Figs. 11a and 11b is that the time taken to reach temporal peak upsurges as ε_0 or *M* increases and reverse trend is noticed for β or *N*. From the Figs. 11c, it is clear that, as $Br\Theta^{-1}$ or Gr rises, the Bejan number upsurges. Here, the notable remark in these figures is the time to attain temporal peak, and time-independent state is almost similar as *Gr* or $Br\Theta^{-1}$ upsurges.

Fig. 12 demonstrates the time-independent state *Be* against the radial direction at *X* = 1.0 for various parameter values. The effects of β & ε_0, *M* & *N* and $Br\Theta^{-1}$ & *Gr* on *Be* along the radial direction at *X* = 1.0 are shown in Figs. 12a-c, respectively. Here in all these figures, the steady-state characteristics of Bejan number are almost similar to time-independent state entropy generation (*Ns*) which is shown in the Figs. 10a – 10c. From Fig. 12a as β or ε_0 increases it is seen that the steady-state *Be* increased in the interval $R \in (1, 5.6)$, decreases in the interval $R \geq 5.6$. Similarly, in the Figs. 12b and 12c, it is noted that for augmenting values of *M* or *N* and $Br\Theta^{-1}$ or *Gr*, the *Be* curves increases. From Figs. 10 and 12, it is clearly evident the steady-state entropy production is more than the Bejan number near the wall. This confirms that smaller *Be* yields an increase in N_2, i.e., $N_1 < N_2$ (Refer equation (21)) and thus irreversibility due to heat transfer is dominated by fluid friction which gives more entropy production in the vicinity of the plate.

Figs. 13a-c represents the entropy lines for different values of β, ε_0, *M*, *N*, $Br\Theta^{-1}$ and *Gr*. In Fig. 13a, the variation of β is shown between (i) and (ii); & ε_0 between (ii) and (iii). Similarly, in Fig. 13b, the variation of the *M* is shown between (i) and (ii); & *N* between (ii) and (iii). Also in Fig. 13c, the variation of $Br\Theta^{-1}$ is shown between (i) and (ii); & *Gr* between

(ii) and (iii). Few important observations are noted here from all these figures. The variation of entropy lines occurs very close to the hot cylinder wall for increasing the values of β, ε_0, *M*, *N*, $Br\Theta^{-1}$ and *Gr*. From Figs. 13a and 13c [(i), (ii) and (iii)] it can be observed that, the entropy lines moving away from the hot wall as β, ε_0, *M*, *N*, $Br\Theta^{-1}$ and *Gr* increases. Similarly, in Fig. 13b [(i), (ii) & (iii)], the entropy lines becoming close to the hot wall as *M* or *N* increases. The entropy production occurs in the neighbourhood of the hot cylinder wall for all values of β, ε_0, *M*, *N*, $Br\Theta^{-1}$ and *Gr*.

In the same way, the Bejan lines for different values of control parameters are shown in Figs. 14a – 14c. For all values of β, ε_0, *M*, *N*, $Br\Theta^{-1}$ and *Gr*, it is observed that the variation of Bejan lines occur in the proximity of the hot cylindrical wall only. From Fig. 14a it is seen that, the Bejan lines are becoming closer to the hot wall as β increases and reverse trend is noticed for ε_0. Also, in Figs. 14b and 14c the Bejan lines becoming close to the hot wall as *M* or *N* or $Br\Theta^{-1}$ or *Gr* increases. Hence, the Bejan production occurs in the neighbourhood of the hot cylinder wall only.

Tables 3a-b tabulates the differences between Casson and Newtonian fluid flows for the flow-field variables with their temporal peak and the time-independent state values for β, ε_0, *M*, *N*, $Br\Theta^{-1}$ and *Gr,* respectively. For a Casson fluid, all flow control parameters except magnetic parameter, the time required to attain the temporal peak is higher than the usual Newtonian fluid. Similarly, the steady-state time of Newtonian fluid for *U*, θ, *Ns* and *Be* is more compared to the Casson fluid. Also, the peak velocity values occur at $X = 1.0$ for all control parameters and these values of Casson fluid are smaller compared with those of Newtonian fluid.

Tables 4a-b summarized the average momentum and heat transport coefficients of Casson fluid and Newtonian fluid for various non-dimensional parameters, respectively. From Tables 4a and 4b, it is observed that the values of the skin-friction coefficient of Casson fluid are larger compared to the Newtonian fluid while the opposite trend is evident in average Nusselt number. Hence, the characteristics of average momentum and heat transport coefficients of Casson fluid significantly vary from that of the Newtonian fluid.

Figs. 15a and 15b illustrate the *U* and θ contours for Casson and Newtonian fluid flows, respectively. At any given point of location in 2D-rectangular region, i.e. $0 < X \leq 1.0$, $1 <$

$R \leq 4.05$, the velocity of the Casson fluid flow is observed to be smaller than the Newtonian fluid flow. While the reverse trend is noticed for the temperature filed at any location in the (*X*, *R*) coordinate system except the boundary points ($X = 0$, $R = 1$ & $R = 20$). Also, the time-independent state velocity and temperature contours for a Casson fluid are slightly different from the denser momentum and thermal boundary layers of Newtonian fluids, respectively.

5. Concluding remarks

The distribution of entropy generation due to the thermal radiative heat transfer for time-dependent flow of a hydromagnetic Casson fluid past a uniformly heated vertical cylinder has been studied numerically. The Crank-Nicolson technique is applied to elucidate the governing flow-field mathematical equations. The entropy generation and Bejan numbers for thermal radiation, including the effects of MHD are derived and evaluated with the help of flow variables. The influences of average values of momentum and heat transport coefficients, entropy generation and Bejan number, as well as the steady-state flow variables are discussed in detail. In the present study, the effect of the Casson fluid parameter, viscous dissipation parameter, magnetic parameter, radiation parameter, group parameter and the Grashof number on entropy generation and Bejan numbers are demonstrated and analysed. Few important conclusions are listed below:

1. The time to accomplish the steady-state for U, θ, Ns and Be amplifies as β or M or N or $Br\Theta^{-1}$ or Gr upsurges and the reverse trend is observed for ε_0.
2. The velocity increases and temperature decrease with rising the values of β. Also, the $\overline{C_f}$ decreases with augmenting values of β. Similarly, the $\overline{Nu}$ increases with increasing values of β.
3. Entropy heat generation parameter and Bejan number increases for increasing values of β or ε_0 or $Br\Theta^{-1}$ or Gr and the reverse trend is seen for M or N.

4. The time to attain the temporal peak for *Ns* is same as β or ε_0 rises. Also, it decreases for increasing values of $Br\Theta^{-1}$ and *Gr*.
5. The transient and steady-state results of flow variables, average heat and momentum transport coefficients, entropy production, Bejan number for non-Newtonian Casson fluid differs with the Newtonian fluids.

Nomenclature

Be	dimensionless Bejan number
B_0	applied magnetic field (kg. s^{-2}. A^{-1})
Br	Brinkman number
B	magnetic flux (Wb)
c_p	specific heat at constant pressure (J.kg^{-1}. K^{-1})
E	electric field (V. m^{-1})
$\overline{C_f}$	dimensionless average momentum transport coefficient
g	acceleration due to gravity (m.s^{-2})
Gr	Grashof number
H	magnetic field (kg. s^{-2}. A^{-1})
J	current density (A.m^{-2})
k	thermal conductivity (kg·m·s^{-3}·K^{-1})
M	magnetic parameter
N	radiation parameter
Ns	dimensionless entropy heat generation number
$\overline{Nu}$	dimensionless average heat transport coefficient
Pr	Prandtl number
p	fluid pressure (kg.m^{-1}. s^{-2})

q_r radiative heat flux (kg. s^{-3})

U velocity vector (m.s^{-1})

r_o radius of the cylinder (m)

t' time (s)

t dimensionless time

T' temperature (K)

τ_{ij} shear stress tensor (kg.m^{-1}. s^{-2})

x axial coordinate (m)

r radial coordinate (m)

u, v velocity components in (x, r) coordinate system (m.s^{-1})

X dimensionless axial coordinate

R dimensionless radial coordinate

U, V dimensionless velocity components in X, R directions, respectively

Greek letters

θ dimensionless temperature

α thermal diffusivity (m^2·s^{-1})

β Casson fluid parameter

ε_0 viscous dissipation parameter

β_T volumetric coefficient of thermal expansion (K^{-1})

σ electrical conductivity of the fluid (kg^{-1}. m^{-3}. s^3. A^2)

κ^* mean absorption coefficient (kg^{-1}.m^{-3}. s^3. W)

σ^* Stefan-Boltzmann constant (W.m^{-2}. K^{-4})

ρ density (kg·m^{-3})

υ kinematic viscosity (m^2. s^{-1})

μ viscosity of the fluid (kg.m^{-1}. s^{-1})

Θ dimensionless temperature difference

$Br\Theta^{-1}$ dimensionless group parameter

Subscripts

w wall conditions

l, m grid levels in (X, R) coordinate system

∞ ambient conditions

Superscript

n time level

Acknowledgements

The third author wishes to thank DST-INSPIRE (Code No. IF160028) for the grant of research fellowship and to Central University of Karnataka for providing the research facilities.

References

1. Sparrow, E. M. and Gregg, J. L.: Laminar free convection heat transfer from the outer surface of a vertical circular cylinder. ASME Journal of Heat Transfer 78(8), 1823-1829 (1956).
2. Lee, H. R., Chen, T. S. and Armaly, B. F.: Natural convection along slender vertical cylinders with variable surface temperature. ASME Journal of Heat Transfer 110, 103-108(1988).
3. Rani, H. P. and Reddy, G. J.: Soret and Dufour effects on transient double diffusive free convection of couple-stress fluid past a vertical cylinder. Journal of Applied Fluid Mechanics 6(4), 545-554 (2013).
4. Hirschhorn, J., Madsen, M., Mastroberardino, A. and Siddique, J. I.: Magnetohydrodynamic boundary layer slip flow and heat transfer of power law fluid over a flat plate. Journal of Applied Fluid Mechanics 9(1), 11-17 (2016).

5. Dash, R. K., Mehta, K. N. and Jayaraman, G.: Casson fluid flow in a pipe filled with a homogeneous porous medium. International Journal of Engineering Science 34, 1145-1156 (1996).
6. Abbas, Z., Sheikh, M. and Motsa, S. S.: Numerical solution of binary chemical reaction on stagnation point flow of Casson fluid over a stretching/shrinking sheet with thermal radiation. Energy 95, 12-20 (2016).
7. Mustafa, M., Hayat, T., Pop, I. and Hendi, A.: Stagnation-point flow and heat transfer of a Casson fluid towards a stretching sheet. Zeitschrift fur Naturforschung 67, 70-76 (2012).
8. Mythili, D. and Sivaraj, R.: Influence of higher order chemical reaction and nonuniform heat source/sink on Casson fluid flow over a vertical cone and flat plate. Journal of Molecular Liquids 216, 466-475 (2016).
9. Das, M., Mahato, R. and Nandkeolyar, R.: Newtonian heating effect on unsteady hydromagnetic Casson fluid flow past a flat plate with heat and mass transfer. Alexandria Engineering Journal 54, 871-879 (2015).
10. Nadeem, S., Haq, R. U. and Lee, C.: Magnetohydrodynamic flow of a Casson fluid over an exponentially shrinking sheet. Scientia Iranica 19, 1550-1553 (2012).
11. Raju, C. S. K., Hoque, M. M., Anika, N. N., Mamatha, S. U., Sharma, P., Natural convective heat transfer analysis of MHD unsteady Carreau nanofluid over a cone packed with alloy nanoparticles. Powder Technology, 317, 408-416 (2017).
12. Raju, C. S. K., Hoque, M. M., Sivasankar, T., Radiative flow of Casson fluid over moving wedge with gyrotactic microorganism. Advanced Powder Technology, 28, 575-58 (2017).
13. Bejan, A.: The Concept of Irreversibility in Heat Exchanger Design: Counterflow Heat Exchangers for Gas-to-Gas Applications. ASME Journal of Heat Transfer 99, 374-380 (1977).

14. Giangaspero, G. and Sciubba, E: Application of the entropy generation minimization method to a solar heat exchanger: A pseudo-optimization design process based on the analysis of the local entropy generation maps. Energy 58, 52-65 (2013).
15. Badescu,V.: Optimal paths for minimizing lost available work during usual heat transfer processes. Journal of Non-Equilibrium Thermodynamics 29, 53-73 (2004).
16. Kockum, H. and Jernqvist, A: Entropy generation in multifield flows: Equations and Examples of Applications. Institution of Chemical Engineers Trans IChemE 76, 212-222 (1998).
17. Bejan, A.: A study of entropy generation in fundamental convective heat transfer. Journal of Heat Transfer 101, 718-725 (1979).
18. Bejan, A.: Second law analysis in heat transfer. Energy 5, 720-732 (1980).
19. Bejan, A.: Second law analysis in heat transfer and thermal design. Advances in Heat Transfer 15, 1–58 (1982).
20. Omid Mahian, Hakan Oztop, Ioan Pop, Shohel Mahmud, Somchai Wongwises: Entropy generation between two vertical cylinders in the presence of MHD flow subjected to constant wall temperature. International Communications in Heat and Mass Transfer 44, 87–92 (2013).
21. Adnan Saeed Butt, Asif Ali: Entropy analysis of magnetohydrodynamic flow and heat-transfer due to a stretching cylinder. Journal of Taiwan Institute of Chemical Engineers 45, 780-786 (2014).
22. Sufian Munawar, Asif Ali, Ahmer Mehmood: Thermal analysis of the flow over an oscillatory stretching cylinder. Physica Scripta 86(2), 065-401 (2012).
23. Adnan Saeed Butt, Asif Ali, Ahmer Mehmood: Numerical investigation of magnetic field effects on entropy generation in viscous flow over a stretching cylinder embedded in a porous medium. Energy 99, 237-249 (2016).

24. Bassam A.K. Abu-Hijleh: Natural convection heat transfer and entropy generation from a horizontal cylinder with baffles. ASME Journal of Heat Transfer 122(4), 679-692 (2000).

25. Bassam A.K. Abu-Hijleh: Natural convection and entropy generation from a cylinder with high conductivity fins. Numerical Heat Transfer, Part A 39, 405-432 (2001).

26. Bassam A.K. Abu-Hijleh, B.A/K.: Entropy generation due to cross-flow heat transfer from a cylinder covered with an orthotropic porous layer. Heat and Mass Transfer 39, 27-40 (2002).

27. Mirzazadeh M, Shafaei A, Rashidi F: Entropy analysis for non-linear viscoelastic fluid in concentric rotating cylinders. International Journal of Thermal Science 47(12), 1701-1711(2008).

28. Mahian O, Mahmud S, Heris SZ.: Analysis of entropy generation between co- rotating cylinders using nanofluid. Energy 44(1), 438-446 (2012).

29. Bassam A.K. Abu-Hijleh, Waleed N. Heilen: Entropy generation due to laminar natural convection over a heated rotating cylinder. International Journal of Heat and Mass Transfer 42, 4225-4233(1999).

30. Jia Qing, Muhammad Mubashir Bhatti, Munawwar Ali Abbas, Mohammad Mehdi Rashidi and Mohamed El-Sayed Ali: Entropy generation on MHD Casson nanofluid flow over a porous stretching/shrinking surface. Entropy 18(4), 1-14 (2016).

31. Srinivas Jangili, Nagaraju Gajjela, Anwar Beg O.: Mathematical modeling of entropy generation in magnetized micropolar flow between co-rotating cylinders with internal heat generation. Alexandria Engineering Journal 55, pp.1969–1982 (2016).

32. Adnan Saeed Butt and Asif Ali: Entropy analysis of magnetohydrodynamic flow and heat transfer due to a stretching cylinder. Journal of the Taiwan Institute of Chemical Engineers, 45 pp. 780–786(2014).

33. Omid Mahian, Hakan Oztop, Ioan Pop, Shohel Mahmud and Somchai Wongwises: Entropy generation between two vertical cylinders in the presence of MHD flow subjected to constant wall temperature. International Communications in Heat and Mass Transfer, 44, pp. 87–92 (2013).

34. Ramana Murthy, J.V., and Srinivas, J.: Thermodynamic second law analysis of radiative heat transfer in two immiscible micropolar fluids in a channel. Proceedings of the 22nd National and 11th International ISHMT-ASME Heat and Mass Transfer Conference (HMTC1300113), pp. 1-9 (2013).

35. Guillermo Ibáñez, Aracely López, Joel Pantoja and Joel Moreira: Entropy generation analysis of a nanofluid flow in MHD porous microchannel with hydrodynamic slip and thermal radiation. International Journal of Heat and Mass Transfer, 100, pp.89 - 97(2016).

36. Tamoor, M., Waqas, M., Ijaz Khan, M., Ahmed Alsaedi, Hayat, T.: Magnetohydrodynamic flow of Casson fluid over a stretching cylinder. Results in Physics, 7, pp.498–502(2017).

37. Krishnendu Bhattacharyya: MHD stagnation-point flow of Casson fluid and heat transfer over a stretching sheet with thermal radiation. Journal of Thermodynamics, Journal of Thermodynamics, 2013, 1- 9 (2013).

38. Ahmed, N.: Buoyancy induced MHD transient mass transfer flow with thermal radiation. Alexandria Engineering Journal 55(3), 2321–2331 (2016).

39. Gnaneswara Reddy, M.: Unsteady radiative-convective boundary-layer flow of a Casson fluid with variable thermal conductivity. Journal of Engineering Physics and Thermophysics, 88(1), pp. 240-251(2015).

40. Casson, N.: A flow equation for pigment oil suspensions of the printing ink type. In: Rheology of disperse systems. Mill CC (Ed.) Pergamon Press, Oxford 84–102. (1959).

41. Hakeem, A. K. A., Renuka, P., Ganesh, N. V., Kalaivanan, R. and Ganga, B.: Influence of inclined Lorentz forces on boundary layer flow of Casson fluid over an impermeable

stretching sheet with heat transfer. Journal of Magnetism and Magnetic Materials 401, 354-361(2016).

42. M. Q. Brewster, Thermal radiative transfer and properties, John Wiley Sons, New York, 1992.
43. Bejan, A.: Entropy generation minimization. New York, CRC Press, (1996).
44. Rani, H. P., Janardhana Reddy, G. and Kim, C.N.: Transient analysis of diffusive chemical reactive species for couple stress fluid flow over vertical cylinder. Applied Mathematics and Mechanics English Edition 34, 985-1000 (2013).
45. Gnaneswara Reddy, M.: Radiation effects on MHD natural convection flow along a vertical cylinder embedded in a porous medium with variable surface temperature and concentration. Frontiers in Heat and Mass Transfer (FHMT), 5(4), 1-9, (2014).
46. Gnaneswara Reddy, M.: Chemically reactive species and radiation effects on MHD convective flow past a moving vertical cylinder. Ain Shams Engineering Journal, 4, pp. 879–888 (2013).
47. Gnaneswara Reddy, M. and Bhaskar Reddy, N.: Thermal radiation and mass transfer effects on MHD free convection flow past a vertical cylinder with variable surface temperature and concentration. Journal of Naval Architecture and Marine Engineering, June, 6, pp. 1-15(2009).

Table 1. Grid independence test for selecting mesh size.

Grid size	Average skin-friction coefficient ($\overline{C_f}$) for $\varepsilon_0 = 1$, $Pr = 0.71$, $M = 1.0$, $N = 1.0$ and $\beta = 1.0$.	Average Nusselt number ($\overline{Nu}$) for $\varepsilon_0 = 1$, $Pr = 0.71$, $M = 1.0$, $N = 1.0$ and $\beta = 1.0$.
25 × 125	1.0450330	0.5626012
50 × 250	1.0457040	0.5651330
100 × 500	1.0462850	0.5675192
200 × 1000	1.0462980	0.5675245

Table 2. Grid independence test for selecting time step size.

Time step size (Δt)	Average skin-friction coefficient ($\overline{C_f}$) for $\varepsilon_0 = 1$, $Pr = 0.71$, $M = 1.0$, $N = 1.0$ and $\beta = 1.0$.	Average Nusselt number ($\overline{Nu}$) for $\varepsilon_0 = 1$, $Pr = 0.71$, $M = 1.0$, $N = 1.0$ and $\beta = 1.0$.
0.5	1.0462930	0.5675144
0.1	1.0463240	0.5674965
0.08	1.0463300	0.5674935
0.05	1.0463140	0.5675022
0.02	1.0463010	0.5675095
0.01	1.0462850	0.5675192

Table 3. The time required for various variables *U*, θ, *Ns* & *Be* to attain the temporal peak and the time-independent state; the peak velocity for various β, ε_0, *M*, *N*, $\varepsilon_1\Theta^{-1}$ and *Gr* with *Pr* = 0.71 for **(a)** Casson fluid; & **(b)** Newtonian fluid.

β	ε_0 (*M*=*N*=*Gr*=1.0)	Temporal peak time (*t*) of *U*(1, 4.03)	θ(1, 1.34)	*Ns*(1, 2.10)	*Be*(1, 2.10)	Steady-state time (*t*)	Peak value at *X* = 1.0 ***U***	***Ns***	***Be***
(a) Casson fluid									
0.2	1.0	8.34	8.08	0.38		22.70	0.2203	0.4052	
0.5	1.0	7.07	6.76	0.38		23.20	0.2811	0.4534	
1.0	1.0	6.53	6.16	0.38		23.68	0.3137	0.4816	
1.0	2.5	6.41	6.14	0.38		23.35	0.3235	0.3130	
1.0	4.5	6.26	6.09	0.38		22.92	0.3375	0.2452	
0.2	1.0				8.32	11.39			0.0642
0.5	1.0				7.02	15.29			0.0669
1.0	1.0				6.44	18.49			0.0681
1.0	2.5				6.23	16.94			0.0718
1.0	4.5				6.35	18.72			0.0774
M	*N* (ε_0=*Gr*=1.0, β =∞)								
1.0	0.2	5.33	5.13	0.13	10.67	13.35	0.3865	1.0917	0.0859
2.0	0.2			0.13	15.29	16.18	0.2558	0.9547	0.0479
3.0	0.2			0.13	19.59	19.59	0.1901	0.8820	0.0321
1.0	0.4	5.67	5.50	0.22	16.94	16.94	0.3528	0.7324	0.0776
1.0	0.5	5.77	5.73	0.25	18.72	18.72	0.3424	0.6535	0.0751
$Br\Theta^{-1}$	*Gr* (β=ε_0=*M*=*N*=1.0)								
0.3	1.0			6.98		23.68		0.6178	
0.5	1.0			6.95		23.68		0.7540	
1.0	1.0			6.87		23.68		1.0945	
0.1	1.5			6.94		23.40		0.4246	
0.1	2.5			6.58		23.42		0.5192	
$Br\Theta^{-1}$	*Gr* (β=ε_0=*M*=*N*=1.0)								
0.3	1.0				6.44	23.68			0.2043
0.5	1.0				6.44	23.68			0.3405
1.0	1.0				6.44	23.68			0.6810
0.1	1.5				6.36	23.40			0.1601
0.1	2.5				6.14	23.42			0.5191
(b) Newtonian fluid									
β	ε_0 (*M*= *N*=*Gr*=1.0)								
∞	1.0	5.42	5.18	0.33	6.01	24.30	0.3720	0.5282	0.0614
∞	2.5	5.51	5.29	0.33	6.01	24.09	0.3798	0.3751	0.0662
∞	4.5	5.55	5.34	0.33	6.01	23.82	0.3908	0.2944	0.0792
M	*N*								

($\beta = \infty$, $\varepsilon_0 = Gr = 1.0$)									
1.0	0.2	4.80	4.65	0.33	0.12	13.81	0.4444	1.1513	0.0835
2.0	0.2			0.12	0.12	16.29	0.2876	0.9819	0.0453
3.0	0.2			0.12	0.12	19.66	0.2105	0.8964	0.0299
1.0	0.4	5.05	4.82	0.22	0.19	17.29	0.4113	0.7860	0.0769
1.0	0.5	5.21	5.06	0.25	0.21	19.13	0.4010	0.7052	0.0749

Table 4. Comparison between (a) Casson fluid and (b) Newtonian fluid flows for various values of β, ε_0, M, N with respect to the average values of $\overline{C_f}$ and $\overline{Nu}$ with $Pr = 0.71$ & $Gr = 1.0$.

β	ε_0	$\overline{C_f}$	$\overline{Nu}$
(a) Casson fluid			
0.2	1.0	1.6935	0.5186
0.5	1.0	1.2522	0.5499
1.0	1.0	1.0462	0.5675
1.0	2.5	1.0628	0.4921
1.0	4.5	1.0864	0.3826
M	*N*		
1.0	0.2	1.1922	0.4611
2.0	0.2	0.9514	0.4362
3.0	0.2	0.8067	0.4176
1.0	0.4	1.1257	0.5088
1.0	0.5	1.1049	0.5239
(b) Newtonian fluid			
β	ε_0		
∞	1.0	0.7651	0.5956
∞	2.5	0.7732	0.5305
∞	4.5	0.7846	0.4386
M	*N*		
1.0	0.2	0.8494	0.4741
2.0	0.2	0.6722	0.4450
3.0	0.2	0.5668	0.4239
1.0	0.4	0.8117	0.5279
1.0	0.5	0.7996	0.5452

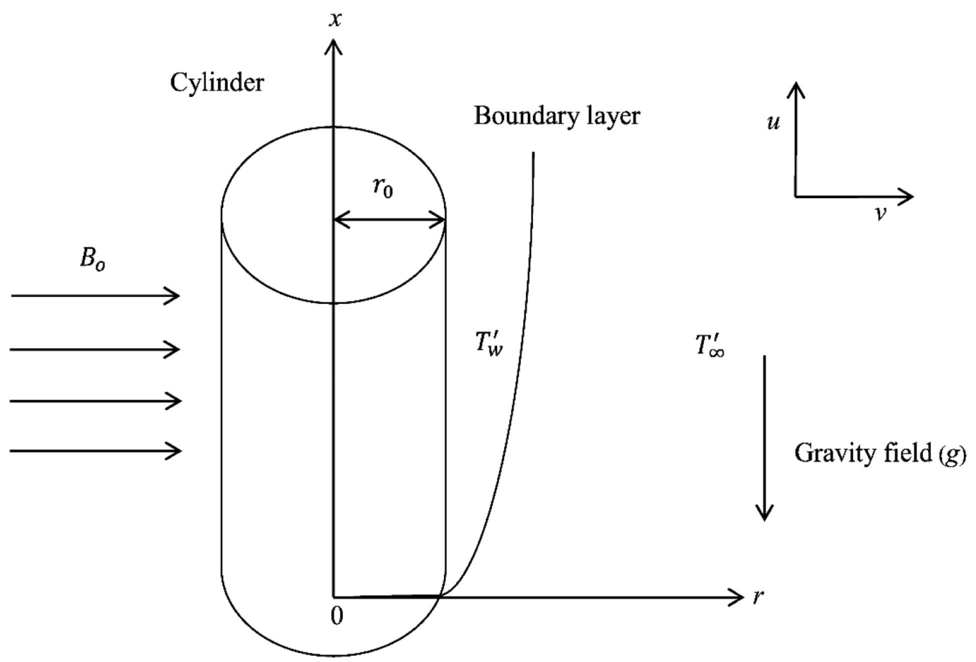

Fig. 1. Schematic of the investigated problem.

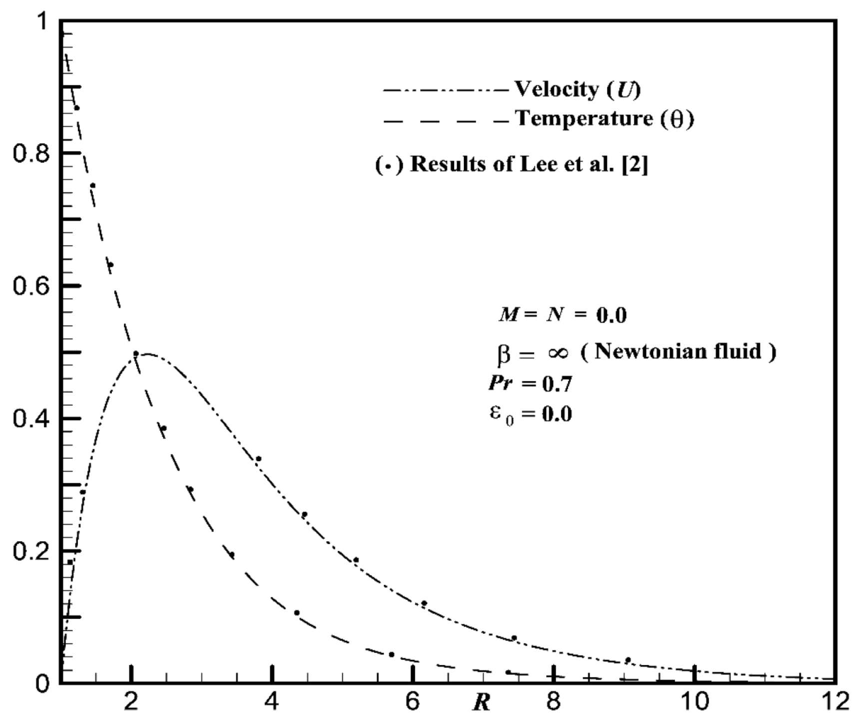

Fig. 2. Comparison of flow-field variables.

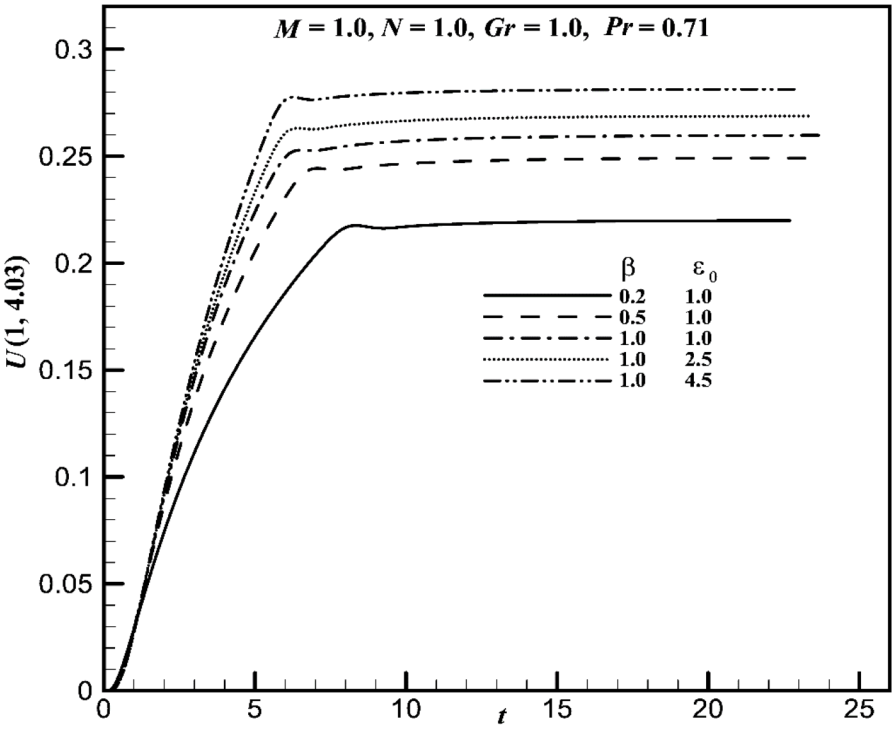

(3a)

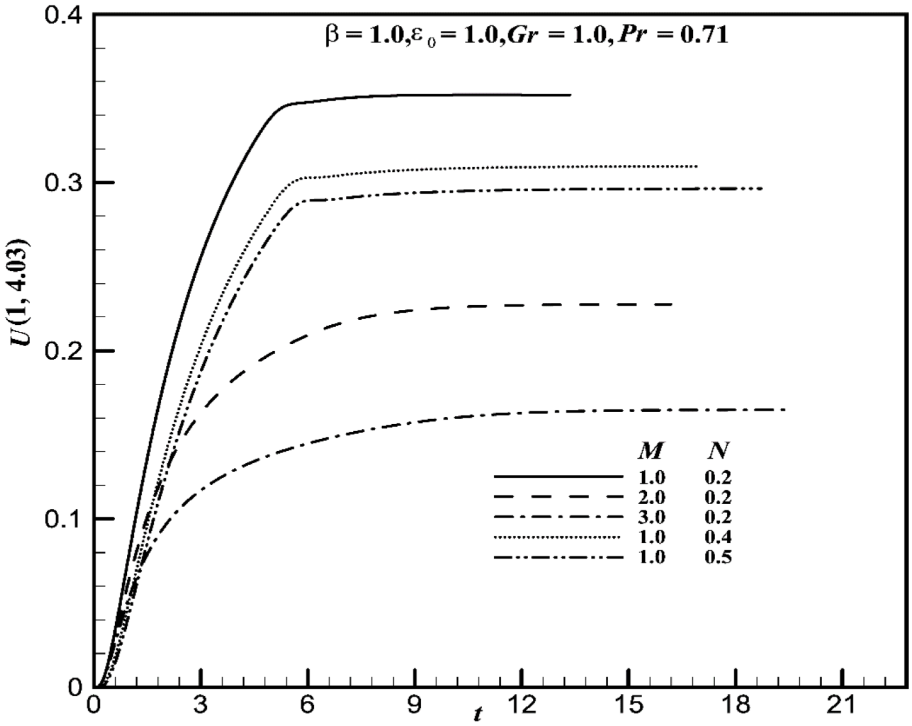

(3b)

Fig. 3. Time-dependent velocity profile (U) versus time (t) at the location (1, 4.03) for the effect of **(a)** β and ε_0; & **(b)** M and N.

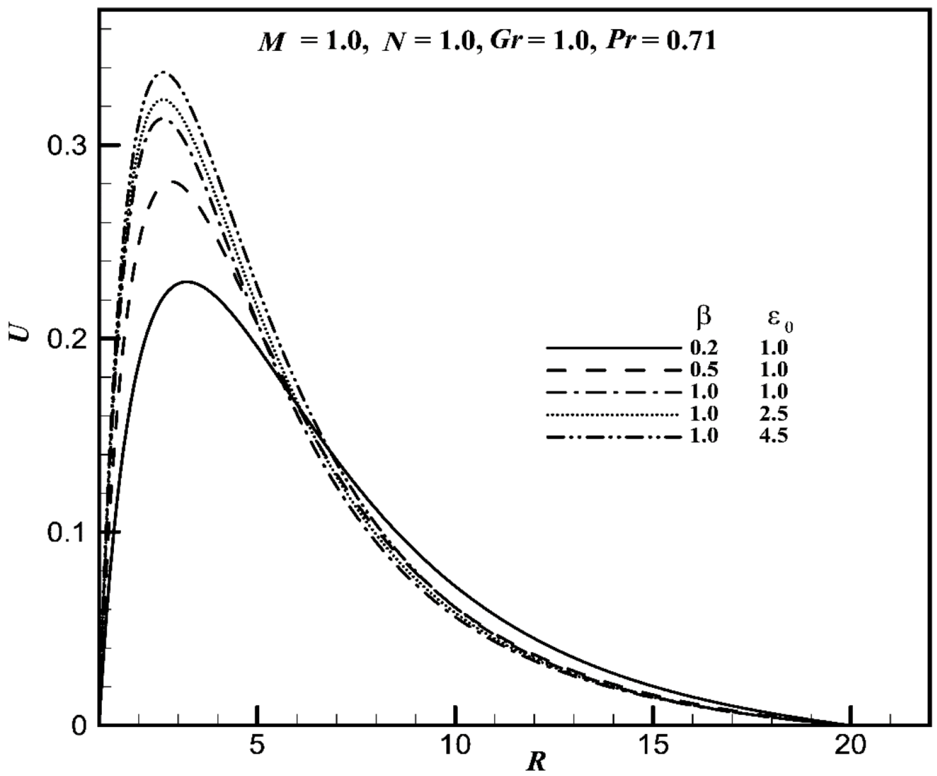

(4a)

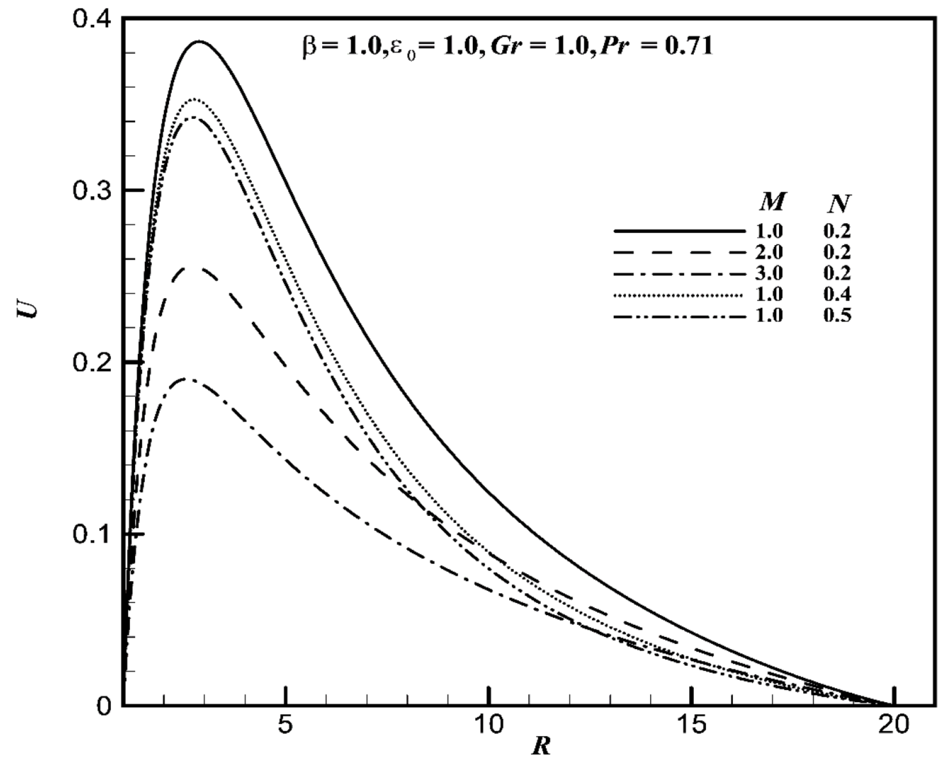

(4b)

Fig. 4. Simulated time-independent state velocity profile (U) versus R at X = 1.0 for the effect of **(a)** β and ε_0; & **(b)** M and N.

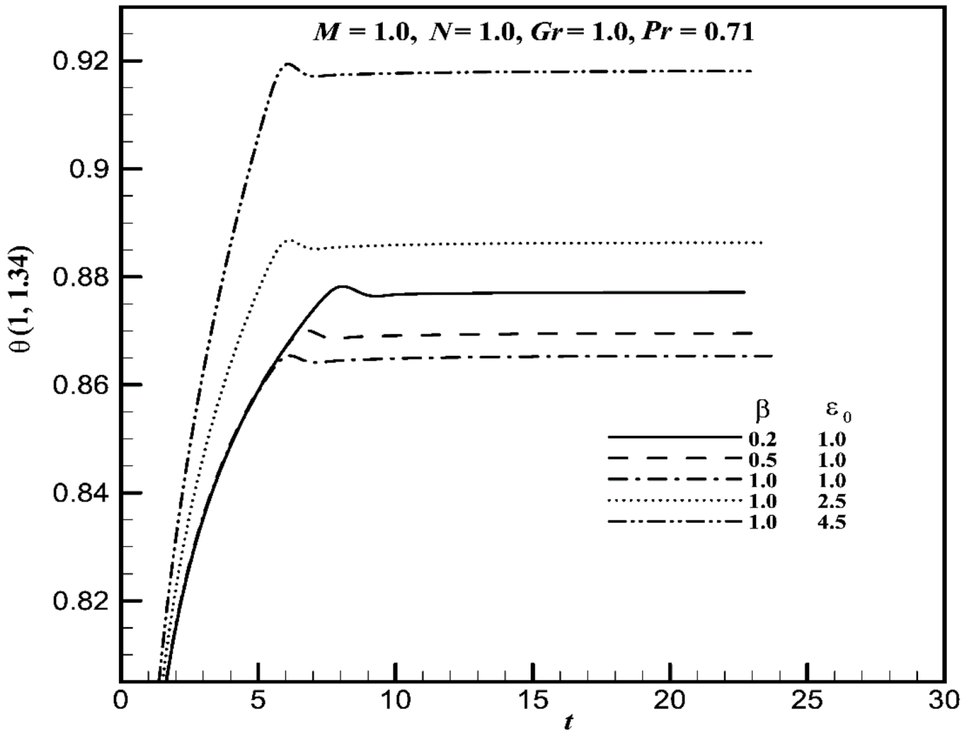

(5a)

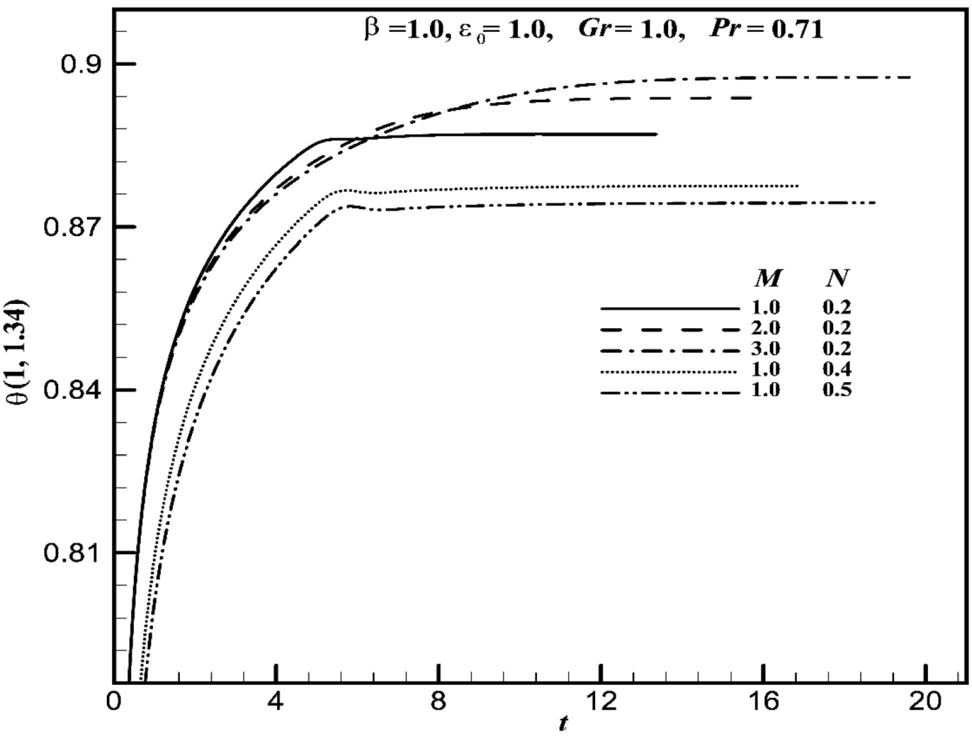

(5b)

Fig. 5. Simulated time-dependent temperature profile (θ) versus time (*t*) at the location (1, 1.34) for the effect of **(a)** β and ε_0; & **(b)** *M* and *N*.

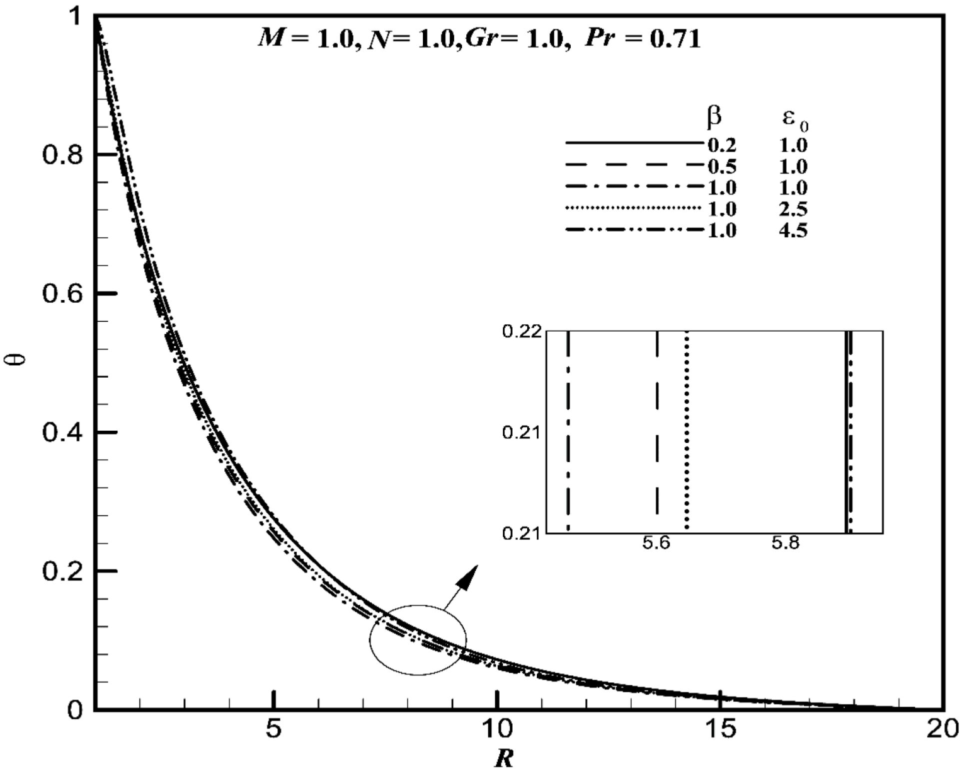

(6a)

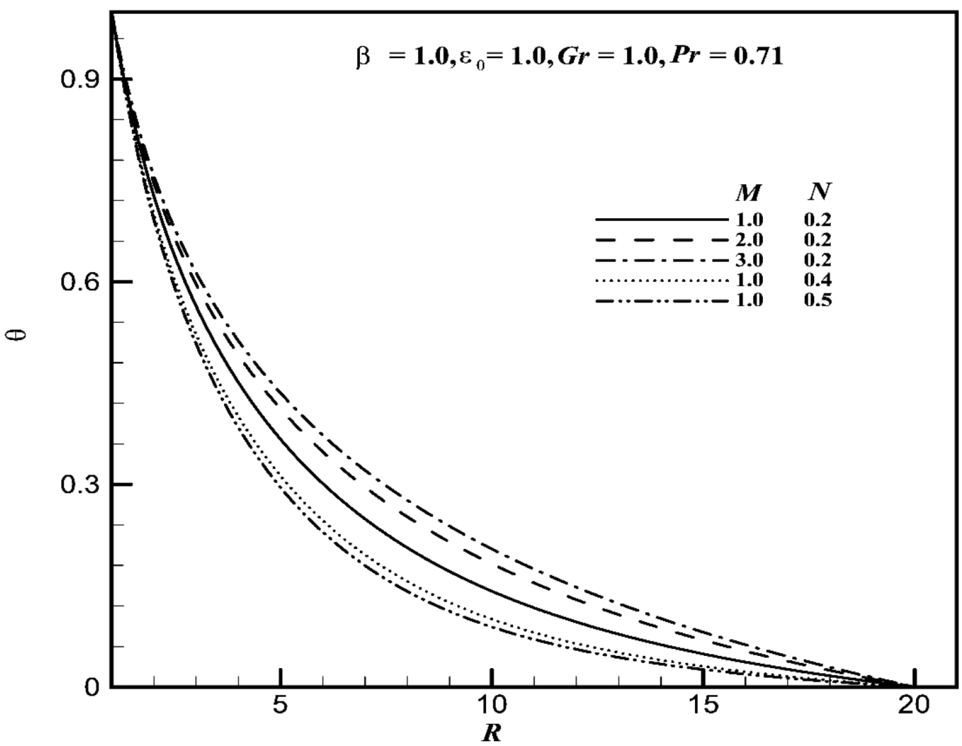

(6b)

Fig. 6. Simulated time-independent state temperature profile (θ) versus R at $X = 1.0$ for the effect of **(a)** β and ε_0; & **(b)** M and N.

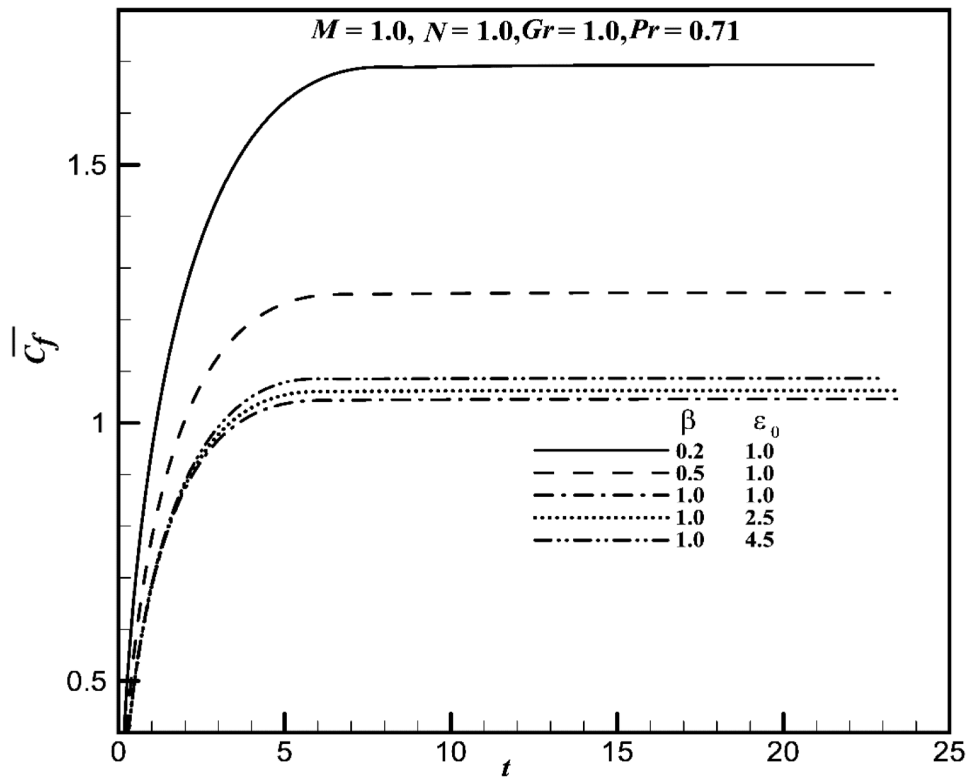

(7a)

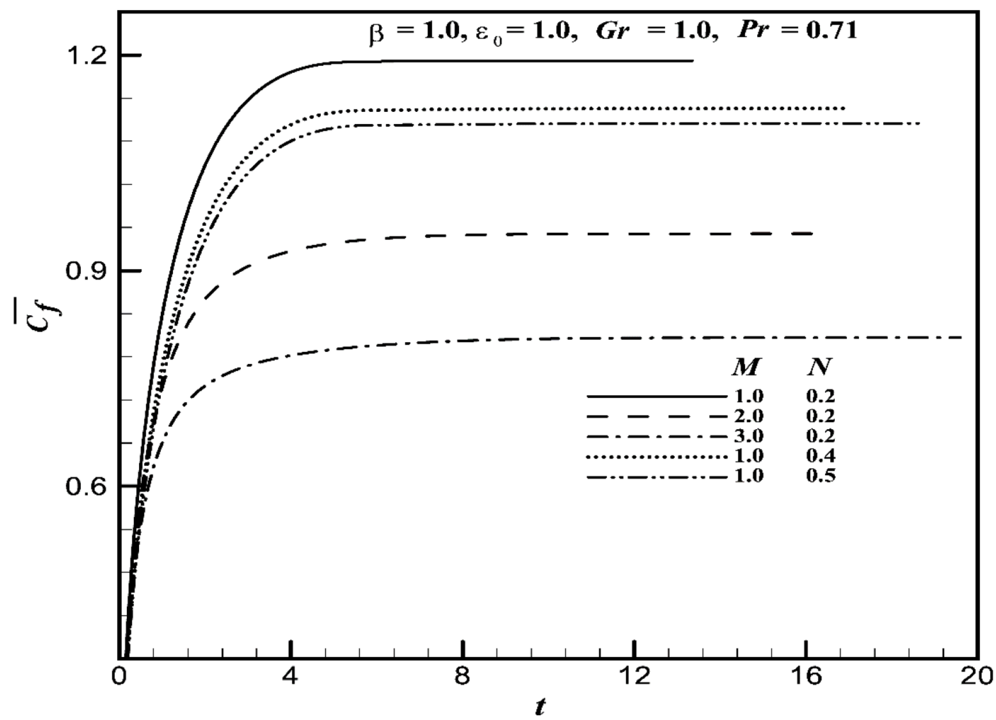

(7b)

Fig. 7. Average momentum transport coefficient ($\overline{C_f}$) for the effect of **(a)** β and ε_0; & **(b)** *M* and *N*.

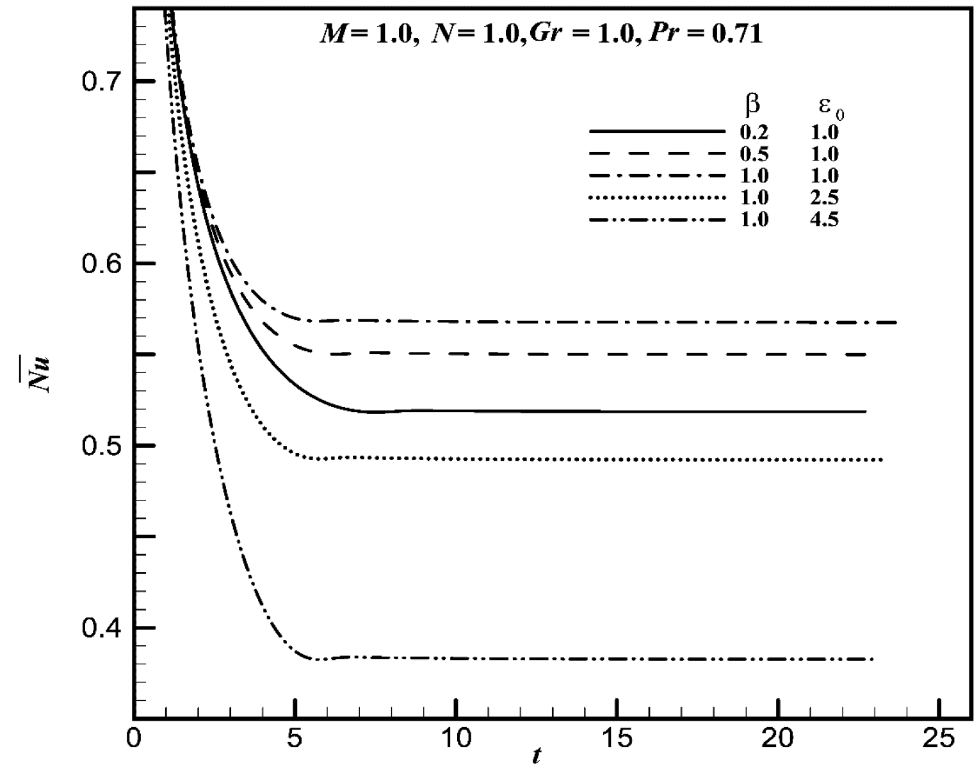

(8a)

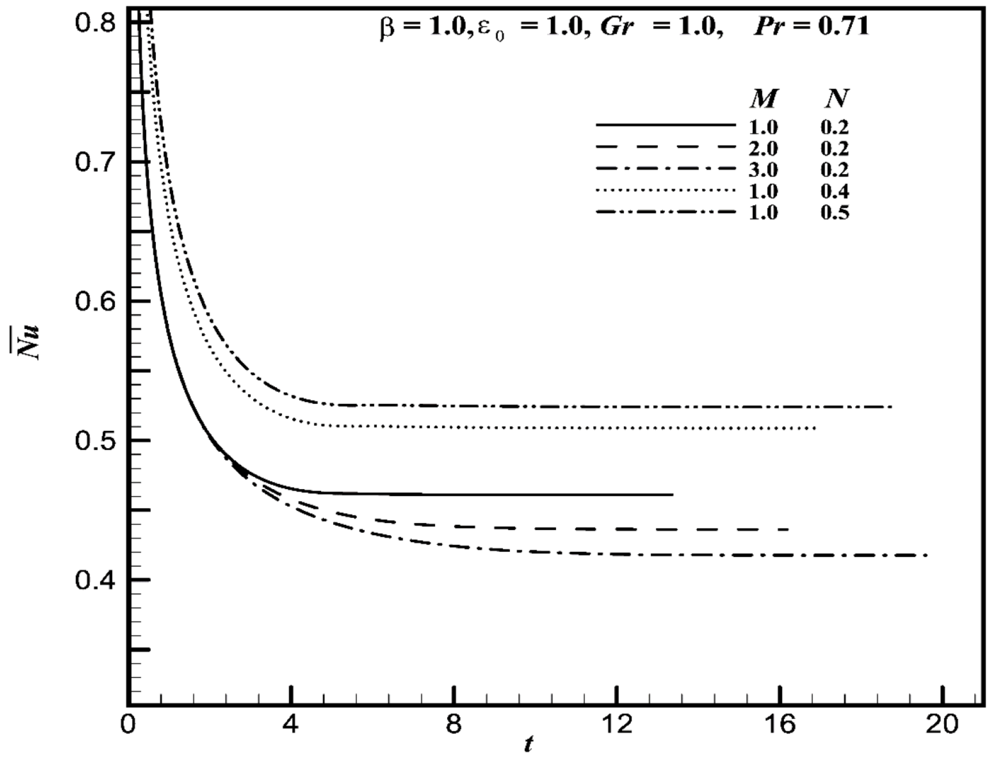

(8b)

Fig. 8. Average heat transport coefficient ($\overline{Nu}$) for the effect of **(a)** β and ε_0; & **(b)** M and N.

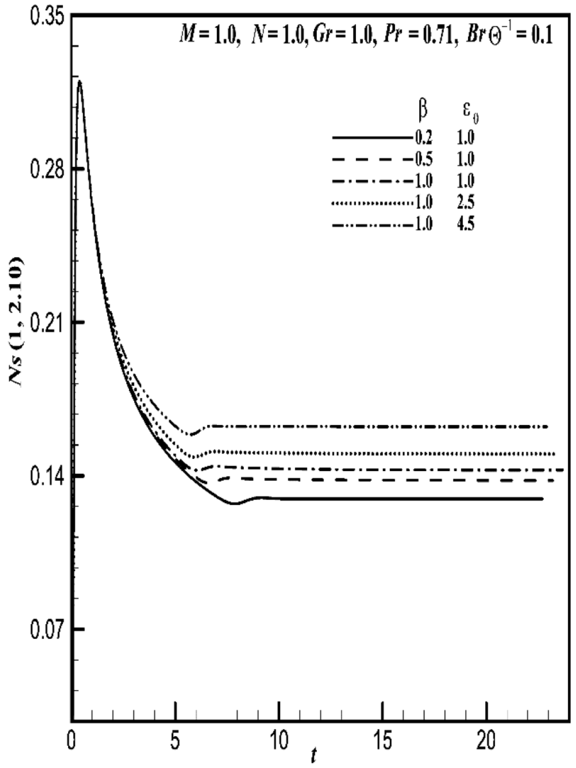

(9a)

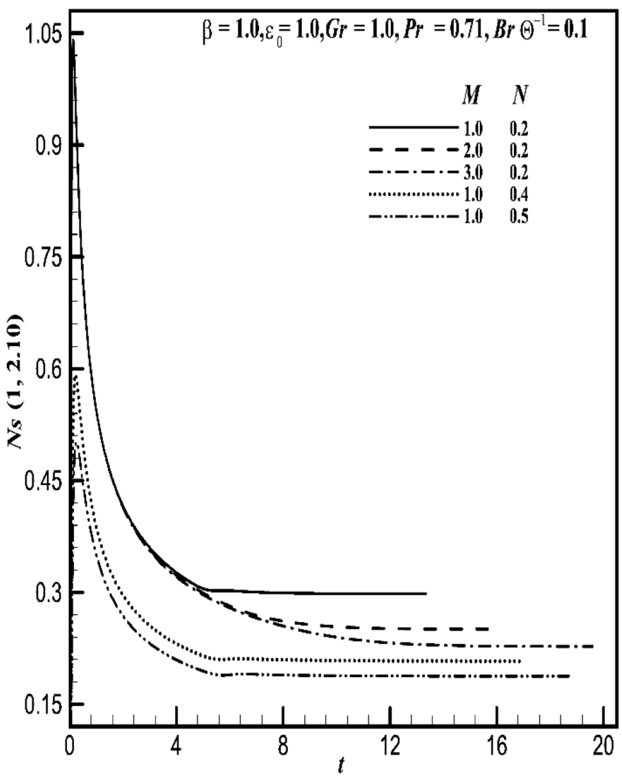

(9b)

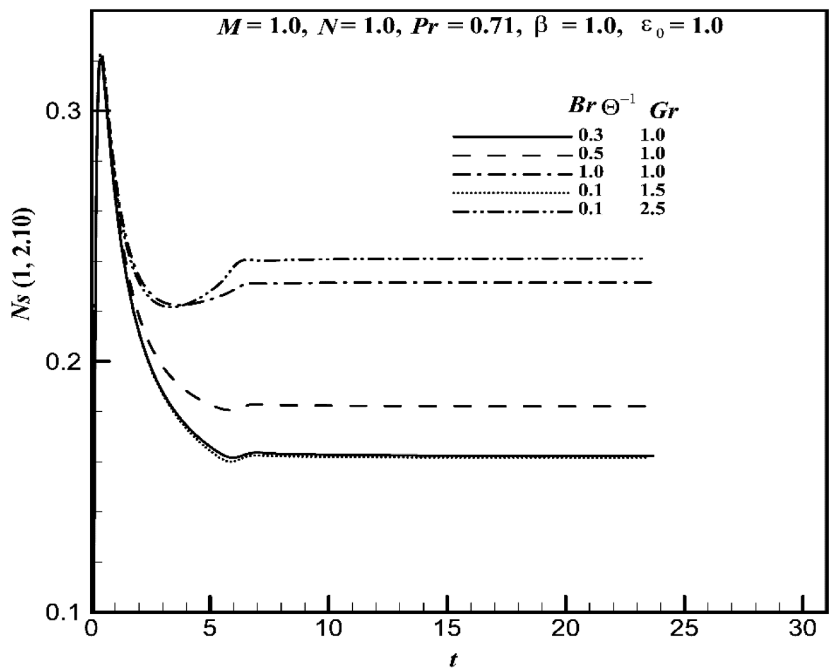

(9c)

Fig. 9. The transient entropy generation number (*Ns*) against time (*t*) for the effect of **(a)** β and ε_0; **(b)** *M* and *N*; & **(c)** $Br\Theta^{-1}$ and *Gr*.

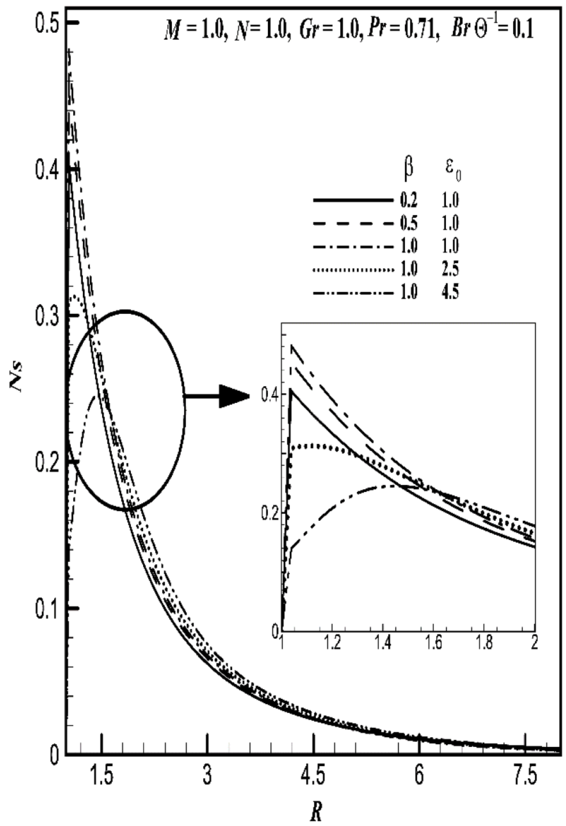

(10a)

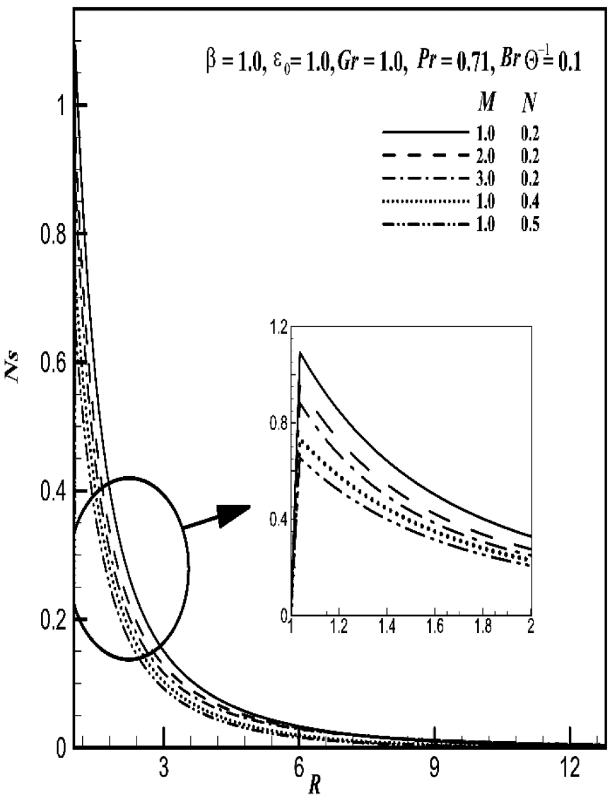

(10b)

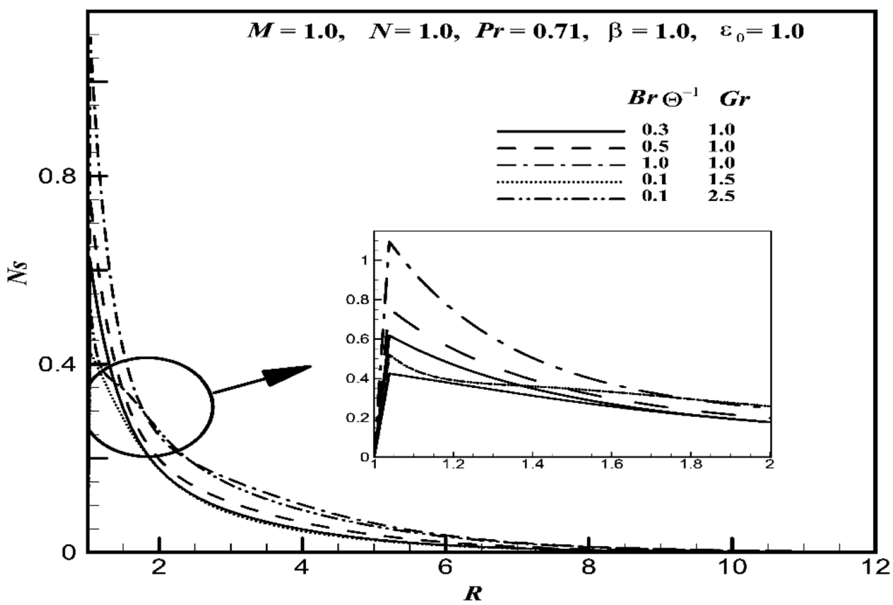

(10c)

Fig. 10. The steady-state entropy generation number (*Ns*) against *R* at *X* = 1.0 for different values of **(a)** β and ε_0; **(b)** *M* and *N*; & **(c)**$Br\Theta^{-1}$ and *Gr*.

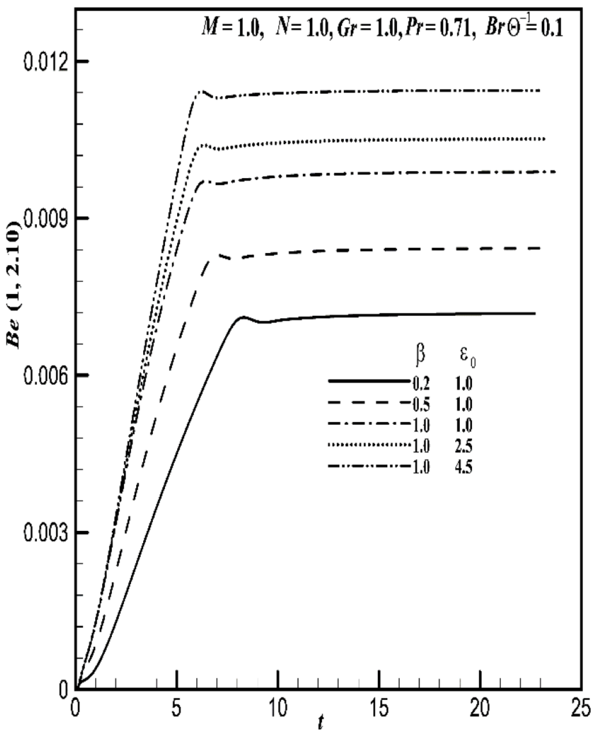

(11a)

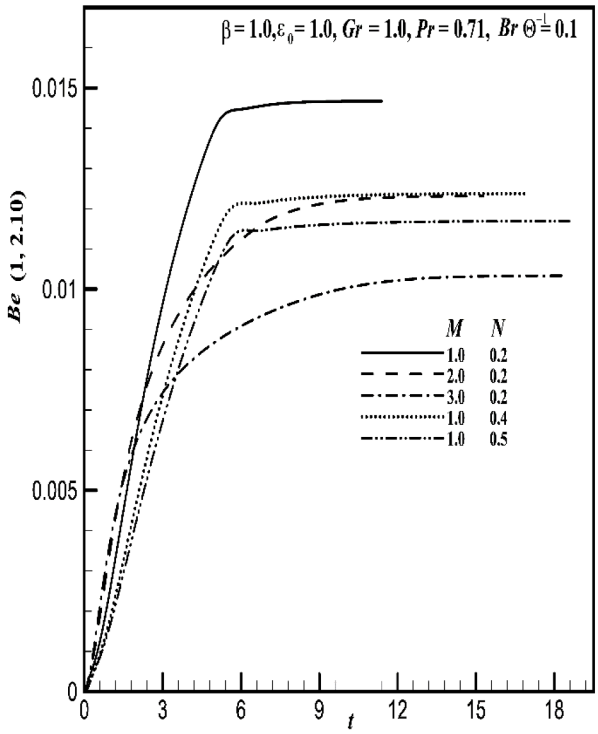

(11b)

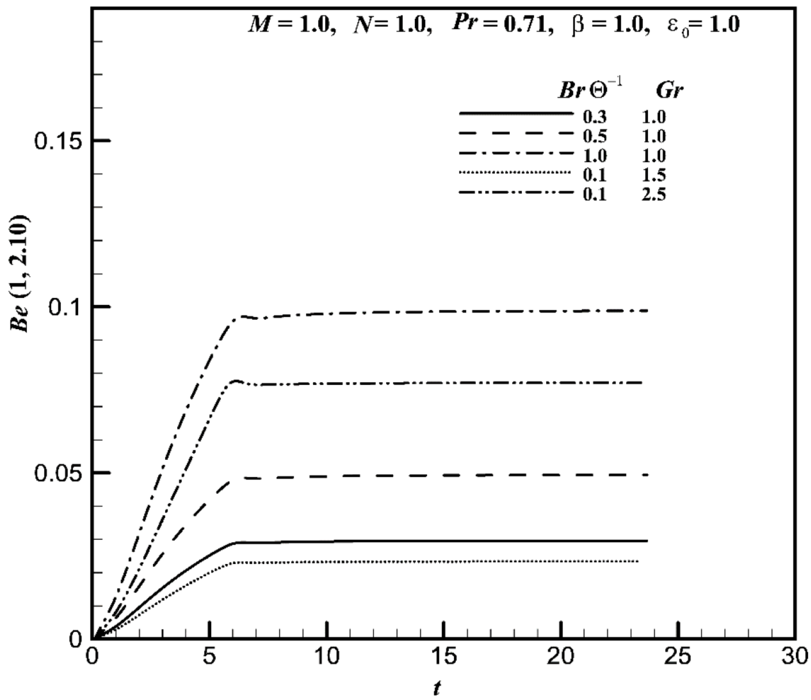

(11c)

Fig. 11. The transient Bejan number (*Be*) against time (*t*) at the point (1, 2.10) for the effect of **(a)** β & ε_0 ; **(b)** *M* and *N*; & **(c)**$Br\Theta^{-1}$ and *Gr*.

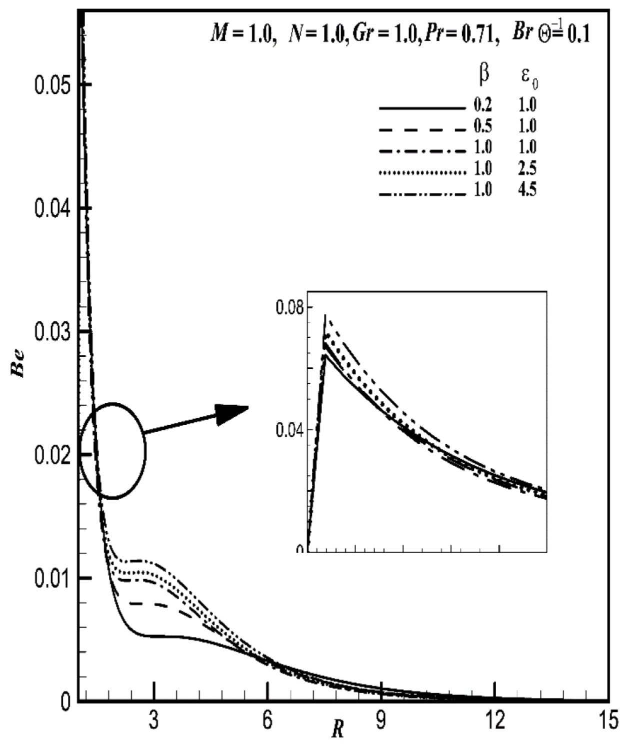

(12a)

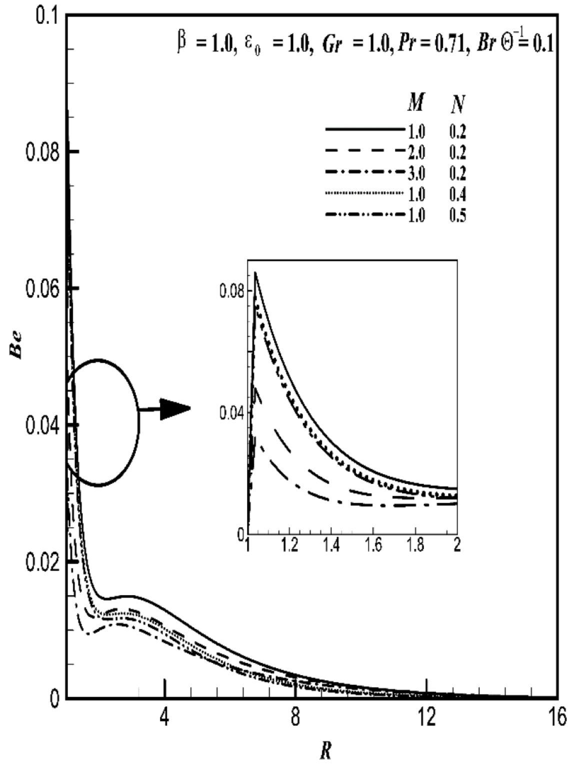

(12b)

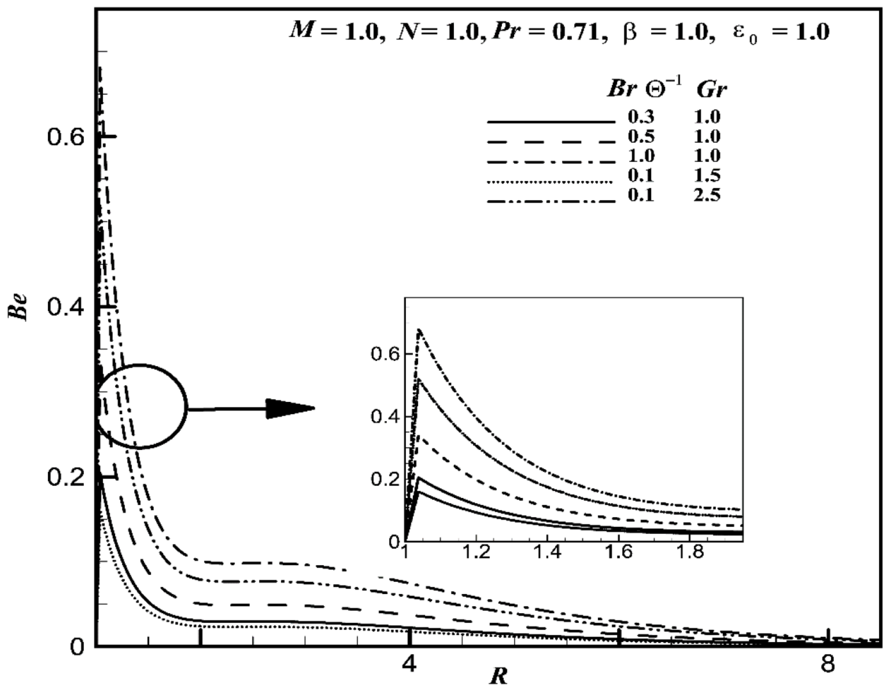

(12c)

Fig. 12. The steady-state Bejan number (*Be*) against *R* for the effect of **(a)** β & ε_0 ; **(b)** *M* and *N*; & **(c)** $Br\Theta^{-1}$ and *Gr*.

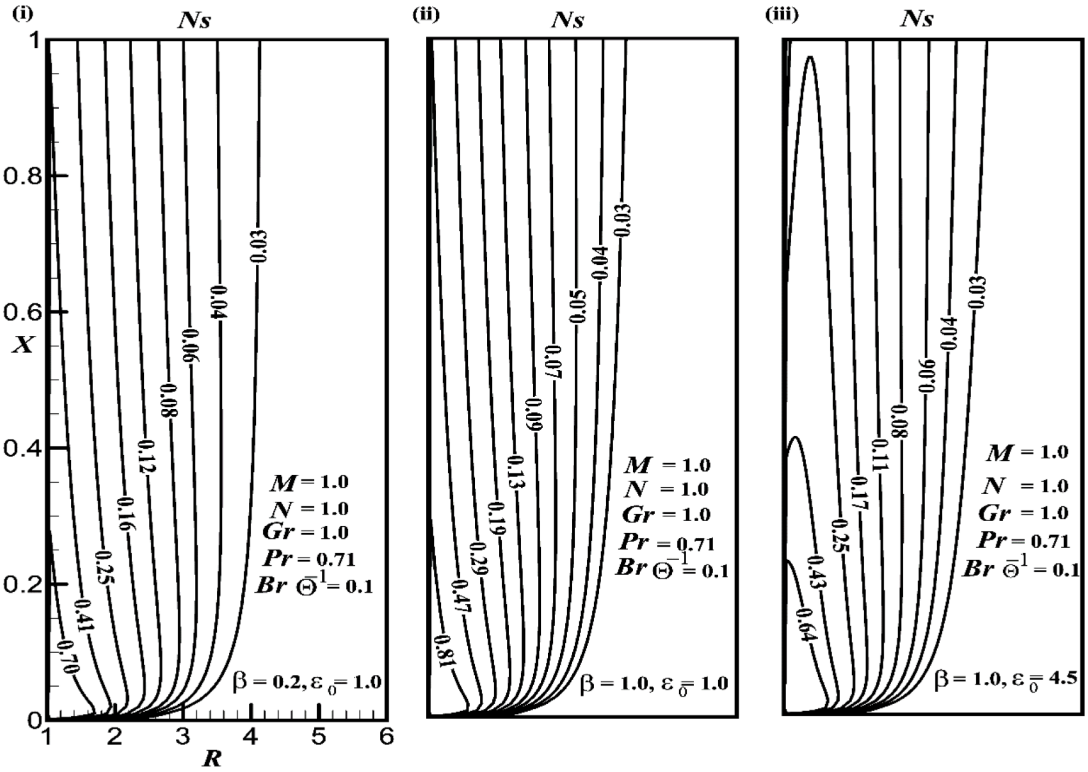
(i)
Ns
(ii)
Ns
(iii)
Ns
X
R
0.70
0.41
0.25
0.16
0.12
0.08
0.06
0.04
0.03
M = 1.0
N = 1.0
Gr = 1.0
Pr = 0.71
Br Θ^{-1} = 0.1
β = 0.2, ε_0 = 1.0
0.81
0.47
0.29
0.19
0.13
0.09
0.07
0.05
0.04
0.03
β = 1.0, ε_0 = 1.0
0.64
0.43
0.25
0.17
0.11
0.08
0.06
0.04
0.03
β = 1.0, ε_0 = 4.5

(13a)

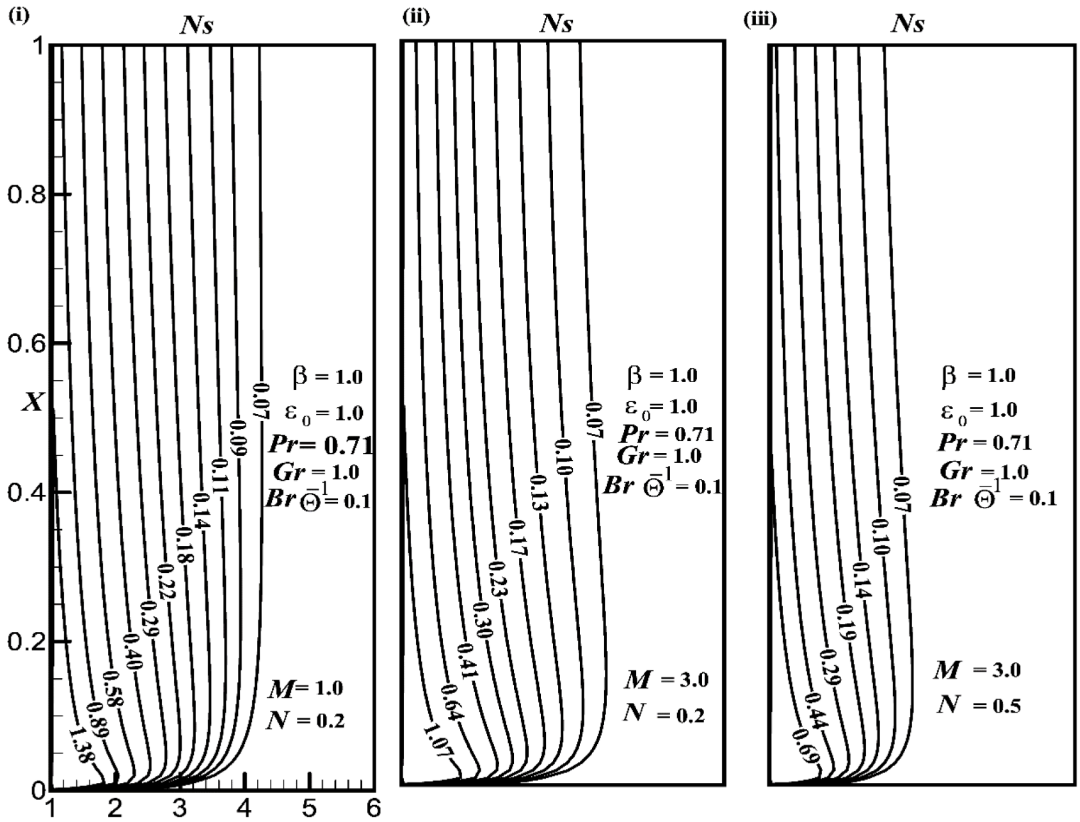
(i)
Ns
(ii)
Ns
(iii)
Ns
X
R
1.38
0.89
0.58
0.40
0.29
0.22
0.18
0.14
0.11
0.09
0.07
β = 1.0
ε_0 = 1.0
Pr = 0.71
Gr = 1.0
Br Θ^{-1} = 0.1
M = 1.0
N = 0.2
1.07
0.64
0.41
0.30
0.23
0.17
0.13
0.10
0.07
M = 3.0
N = 0.2
0.69
0.44
0.29
0.19
0.14
0.10
0.07
M = 3.0
N = 0.5

(13b)

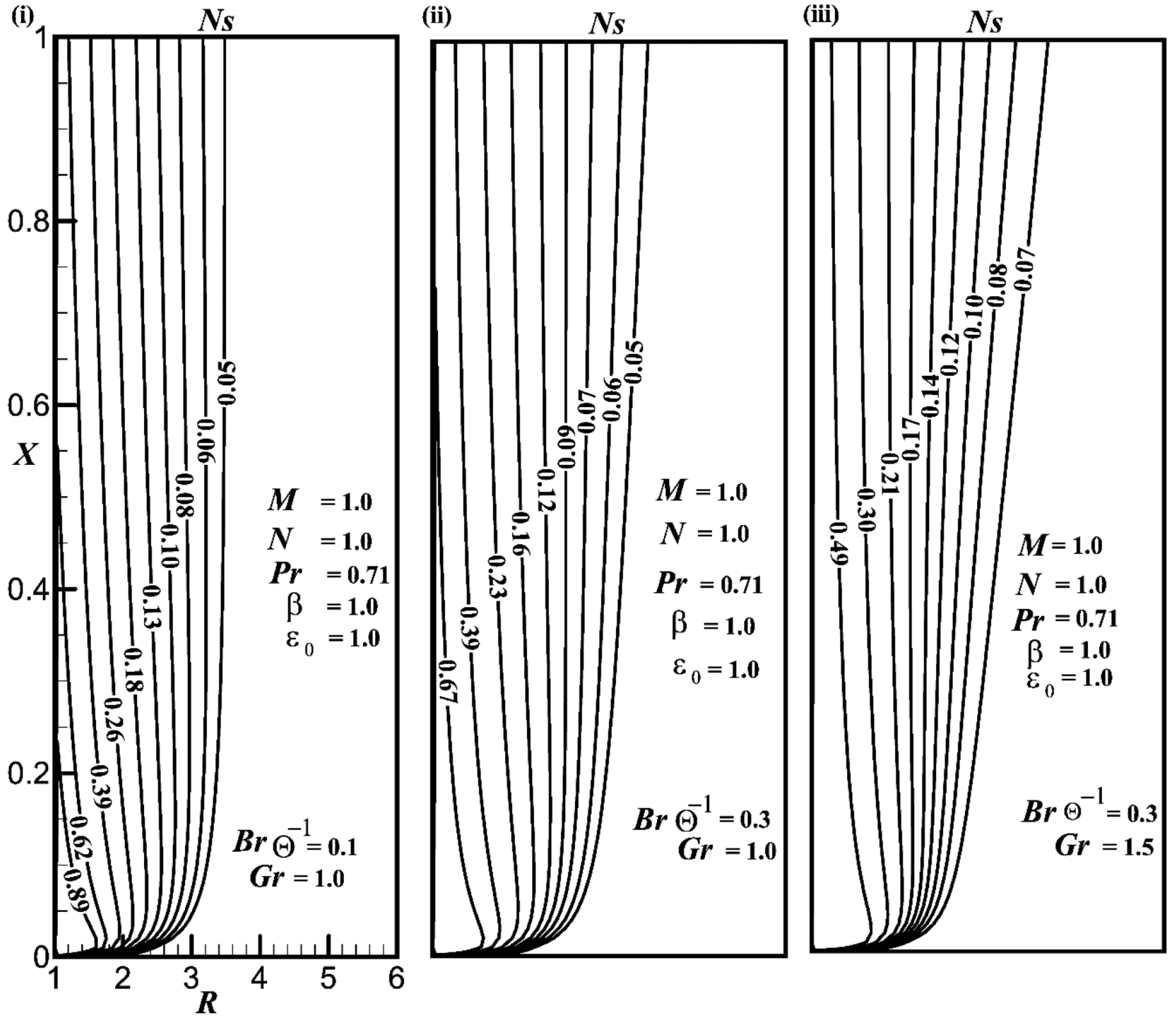

(13c)

Fig. 13. Simulated steady-state entropy lines (*Ns*) in 2D coordinate system (*X*, *R*) for various values of **(a)** β and ε_0; **(b)** *M* and *N*; & **(c)** $Br\Theta^{-1}$ and *Gr*.

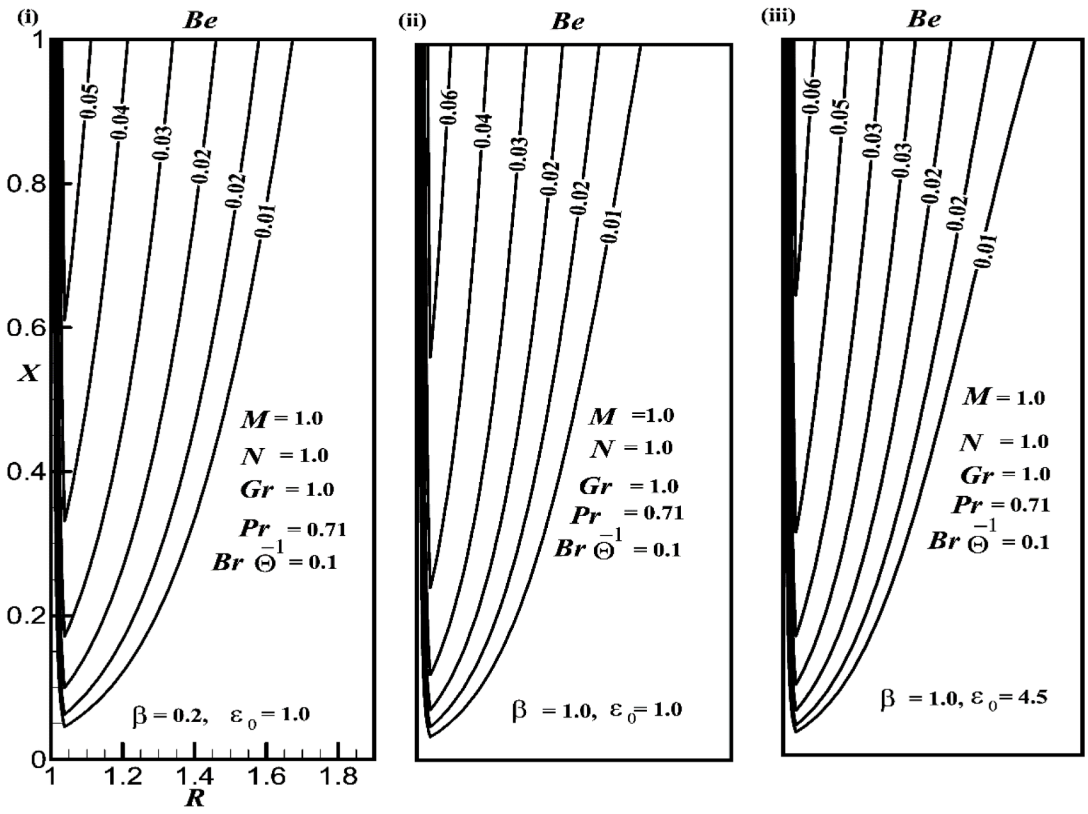
(i)
Be
M = 1.0
N = 1.0
Gr = 1.0
Pr = 0.71
Br Θ^−1 = 0.1
β = 0.2, ε0 = 1.0
(ii)
Be
M = 1.0
N = 1.0
Gr = 1.0
Pr = 0.71
Br Θ^−1 = 0.1
β = 1.0, ε0 = 1.0
(iii)
Be
M = 1.0
N = 1.0
Gr = 1.0
Pr = 0.71
Br Θ^−1 = 0.1
β = 1.0, ε0 = 4.5
X
R

(14a)

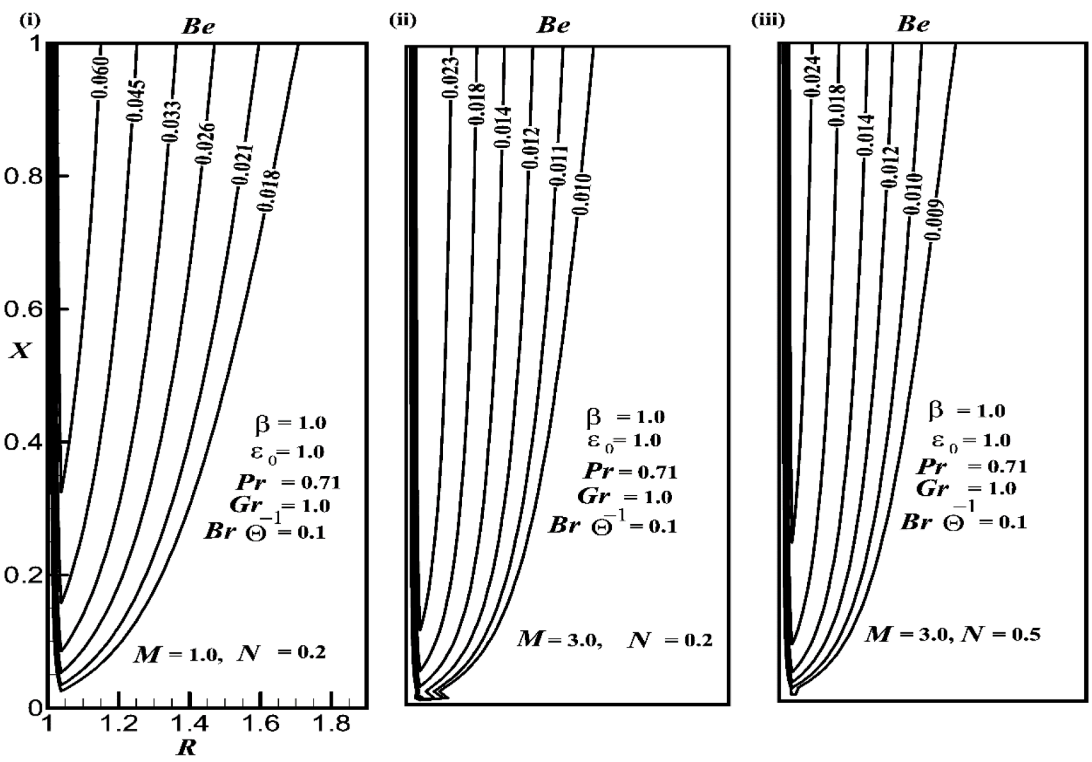
(i)
Be
β = 1.0
ε0 = 1.0
Pr = 0.71
Gr = 1.0
Br Θ^−1 = 0.1
M = 1.0, N = 0.2
(ii)
Be
β = 1.0
ε0 = 1.0
Pr = 0.71
Gr = 1.0
Br Θ^−1 = 0.1
M = 3.0, N = 0.2
(iii)
Be
β = 1.0
ε0 = 1.0
Pr = 0.71
Gr = 1.0
Br Θ^−1 = 0.1
M = 3.0, N = 0.5
X
R

(14b)

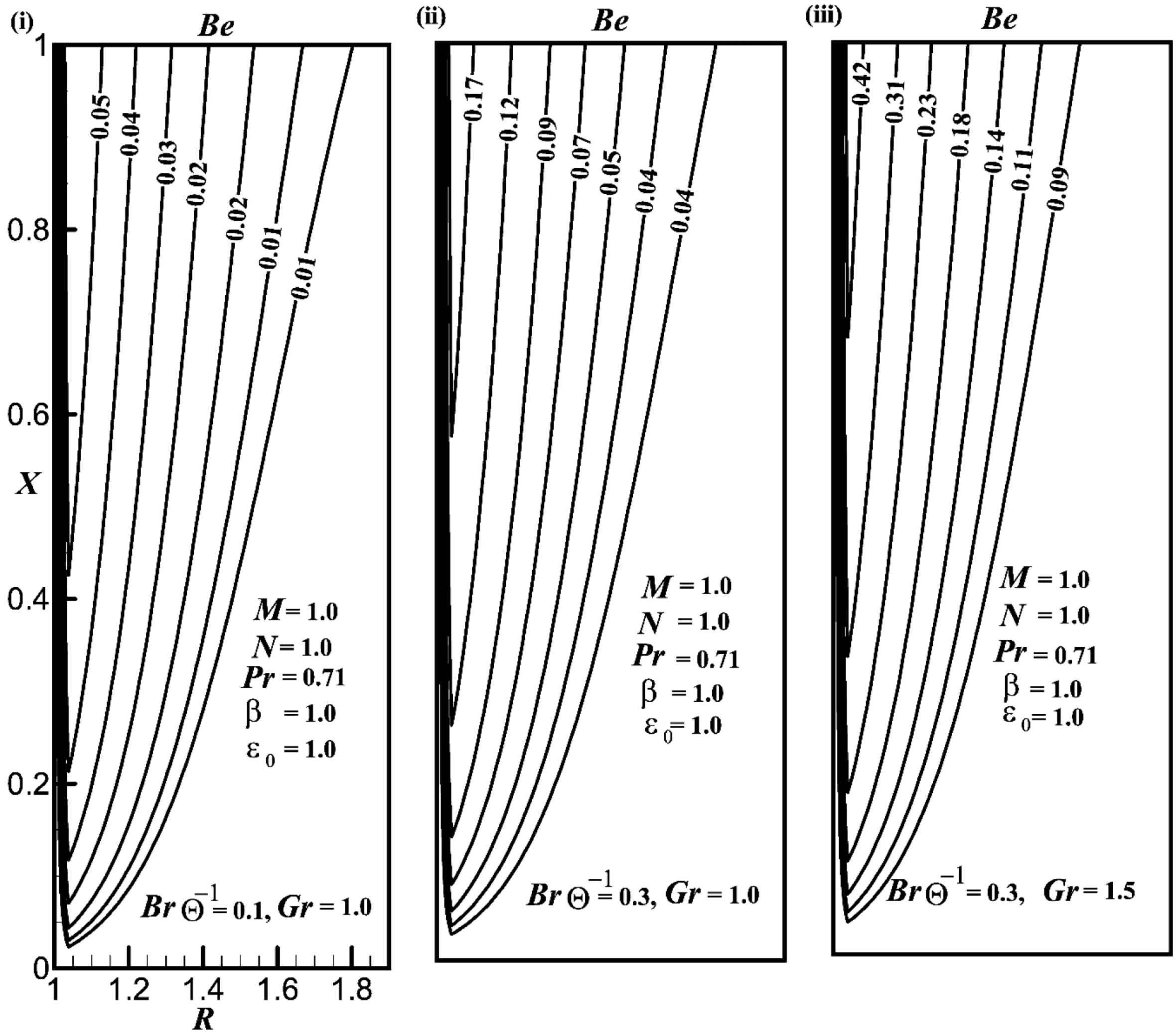

(14c)

Fig. 14. Simulated steady-state Bejan lines (*Be*) in 2D coordinate system (*X*, *R*) for various values of **(a)** β and ε_0; **(b)** *M* and *N*; & **(c)** $Br\Theta^{-1}$ and *Gr*.

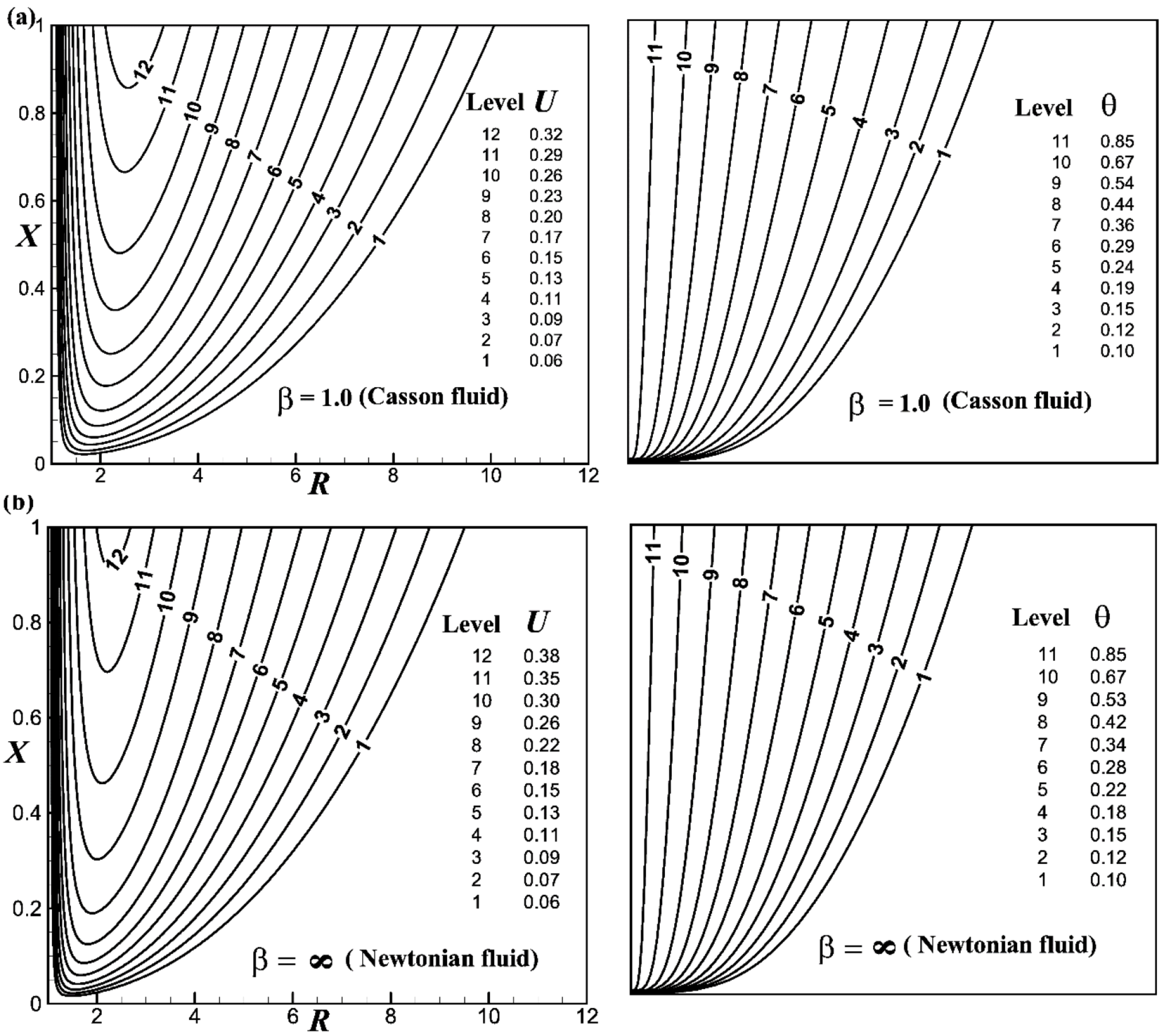

Fig. 15. Time-independent state contours of velocity (U) and temperature (θ) with fixed values of $Pr = 0.71$, $\varepsilon_0 = 4.5$ and $M = N = Gr = 1.0$ for **(a)** Casson fluid ($\beta = 1.0$); & **(b)** Newtonian fluid ($\beta = \infty$).

Highlights

- Hydromagnetic Casson fluid flow over a radiative cylinder has been studied.
- Entropy and Bejan lines are discussed for different values of control parameters.
- Average momentum and heat transport coefficients have been considered.
- Entropy generation upsurges with Casson fluid parameter and Grashof number.
- Flow-field profiles for Casson fluid differs with the Newtonian fluids.